Joining Ferritic SA508 Low Alloy Steel to Austenitic 316L Stainless Steel by Powder Metallurgy via Hot Isostatic Pressing

by

Joshua Le

A thesis submitted to the Graduate Faculty of
Auburn University
in partial fulfillment of the
requirements for the Degree of
Master of Science in Materials Engineering

Auburn, Alabama
December 10, 2022

Keywords: Powder Metallurgy Hot Isostatic Pressing, Dissimilar Metal Joint, Diffusion Simulation, Sensitization

Approved by

Xiaoyuan Lou, Chair, Associate Professor of Materials Engineering
Bart Prorok, Professor of Materials Engineering
Jeffrey Fergus, Professor of Materials Engineering

Abstract

As an alternative to traditional welding, the joining of low alloy steel and austenitic stainless steel using powder metallurgy by hot isostatic pressing was evaluated as a method to join two dissimilar metals. This study examined the microstructure, mechanical properties, and sensitization of two joint designs subjected to a variety of heat treatments: powder SA508 (P508) to bulk 316L (B316L) and powder P316L (P316L) to bulk SA508 (B508). The grain refinement and coarsening induced by solution annealing, normalization, and tempering improved the interface's toughness. The tensile test produced a satisfactory yield strength, and heat treatment reduced the microhardness values along the interface. At the interface between P508-B316L and P316L-B508, however, a notable reduction in impact toughness was observed. The presence of large oxide inclusions at the interface of P508-B316L and the high degree of sensitization on the P316L side of P508-B508 due to the precipitation of chromium-rich carbides ($M_{23}C_6$) caused a reduction in toughness. PanDiffusion was used to simulate the carbon profile and $M_{23}C_6$ carbides as a function of distance to address this issue. By lowering the tempering temperature, the nucleation of carbides was observed to be reduced, but high concentrations of carbides still facilitated the region close to the interface. In conclusion, it was not feasible to join 316L to SA508 by PM-HIP, and a transitional metal, such as a Ni-alloy or a functionally graded material composed of 316L and SA508, is required to minimize carbide precipitation.

Acknowledgments

I would like to start by giving thanks to my mentor and advisor, Dr. Xiaoyuan Lou for his constant guidance, encouragement, discussions, and patience, as well as, for allowing me to join his exceptional research group. He has always pushed me to become a better engineer and has taught me to always question everything. The skills I have learned from working in his group will carry over into the next phase of my career. I will be eternally grateful to you for providing me with the chance to work in advanced manufacturing and for teaching me numerous life lessons.

Also, I am grateful to have worked with my phenomenal group members Dr. Houshang Yin, Jingfan Yang, and Qingyu Pan. They have always taken time out of their busy schedule to assist me and guide me in experiments. I would like to give special thanks to my friend Houshang for his unending assistance and for teaching me the fundamentals of conducting experiments. Furthermore, I would like to express gratitude to my collaborators David Gandy, Victor Samarov, and Raul Rebak for their technical input in the project. Also, I appreciate Dr. Chuan Zhang and Kamal Kadirvel for their response to my Pandat questions and for troubleshooting. In addition, thank you Steve Moore for ensuring the functionality of our laboratory equipment and for maintaining it.

Lastly, I would like to express gratitude to my parents for always being there for me during my undergraduate and graduate studies.

Table of Contents

List of Tables

List of Figures

List of Abbreviations

PWR	Pressure Water Reactor
NNS	Near Net Shaping
NP	Nuclear Power
PM-HIP	Powder Metallurgy by Hot Isostatic Pressing
P508	Powder SA508
P316L	Powder 316L
B508	Bulk SA508
B316L	Bulk SA508
DMJ	Dissimilar Metal Joint
AC	Air Cooling
HT	Heat treatment
WQ	Water Quenching
SA	Solution Annealing
N	Normalization
T	Tempering
OM	Optical Microscope
SEM	Scanning Electron Microscope
EDS	Energy Dispersive X-ray Spectroscopy
UTS	Ultimate Tensile Strength
YS	Yield Strength
CVN	Charpy V-notch
wt%	weight percent

HAZ	Heat affected zone
CTE	Coefficient of thermal expansion
h	hours
CALPHAD	Calculation of Phase Diagram
J	Joules

Chapter 1: Introduction

1.1 Nuclear Reactors

From 1970 to 2022, the expansion of nuclear power capacity has improved steadily over the past 50 years [1]. Currently, the United States is the leading producer of nuclear electricity, accounting for 30 percent of the world's nuclear energy and 19 percent of the nation's electricity [2]. Approximately 61 percent of the nation's energy comes from fossil fuels, while only 20 percent comes from renewable energy [2]. Carbon emissions from nuclear power plants (NPP) are virtually nonexistent; over the lifetime of operation, an NPP will emit between 6 and 8 CO_2e per kilowatt-hour and cost only 5 cents per kilowatt-hour to generate in 2009 [3]. In addition, unlike renewable energy, it is not dependent on the weather or the environment. Therefore, the development of nuclear power is a more cost-effective and environmentally friendly means of reducing the carbon footprint and enhancing the quality of life.

Pressurized water reactor (PWR) is the most utilized reactor and accounts for 70 percent of all reactors [4]. Figure 1 depicts a typical schematic of a PWR. The nozzle-to-safe end, which is the joining of two dissimilar metals, is one of the most essential components of PWRs. These joints are manufactured by forging low alloy steel (LAS), i.e., SA508 grade 3, as the nozzle to piping attached to the reactor vessel, and austenitic stainless steel (ASS), i.e., 316L, as the transitional safe end to piping. A Ni-alloy, such as 600M, is employed as the transitional filler material when arc-welding LAS to ASS to fuse the components. SA508 is chosen for its superior fracture toughness and strength, whereas 316L is chosen for its good strength and outstanding corrosion resistance when in contact with the coolant [5]. The high toughness of SA508 is a result of its ferritic-bainitic microstructure, which is resistant to brittle fracture from neutron embrittlement when the reactor pressure vessel is over-pressurized or from pressurized thermal

shock [3]. Components in nuclear power plants must be able to withstand brittle fracture during operation; therefore, significant efforts have been made in the design, alloy composition, and manufacturing techniques to improve long-term safety and extend operational lifespan.

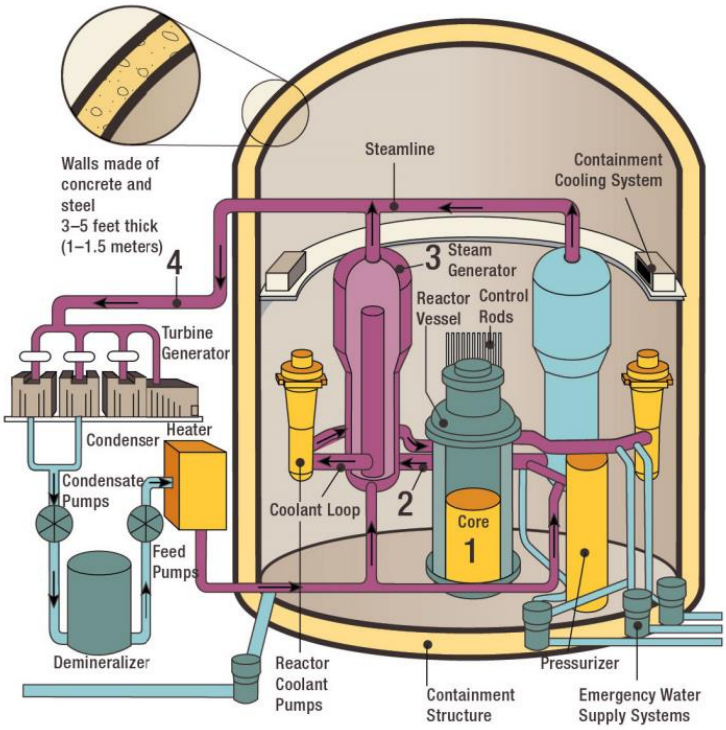

Figure 1. Schematic of a pressurized water reactor [6].

1.2 Problems Associated with Dissimilar Metal Welding

As previously mentioned, welding is widely used to join LAS and ASS; however, the welding process presents several challenges, including the difference in coefficient of thermal expansion (CTE), heat-affected zone (HAZ), intergranular cracking, and inspectability. Anders et al. observed that HAZ is susceptible to failure, as it is the location of crack initiation and propagation due to interdendritic stress corrosion cracking [7]. When two different metals are joined, the considerable difference in chemical composition is the underlying cause of failure.

Since each material has a distinct CTE, this atomic mismatch raises the interfacial stress, leading to premature failure [8-9]. In addition, due to the high heat output of the welding process, atomic diffusion takes place, most notably in carbon. Carbon diffuses as a result of the sudden change in its chemical potential, which provides it with the thermodynamic driving to migrate [10]. As carbon migrates from low alloy steel to austenitic stainless steel, it forms a carbon-depleted zone and a carbon-rich region, as well as new phases. The carbon-rich zone is linked with high hardness, where failure due to embrittlement may occur, whereas the carbon-poor region is characterized by softening.

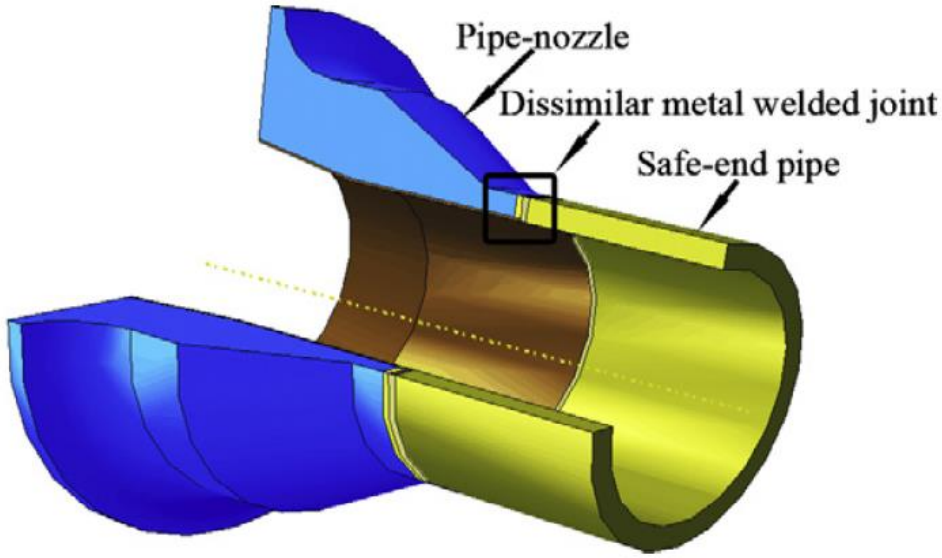

Figure 2. Schematic of the dissimilar metal joint of the nozzle to safe end [6].

Sensitization is characterized by the formation of chromium-rich carbides ($M_{23}C_6$) located preferentially on the grain boundary at temperatures between 500 to 850^{o}C [11]. Since the carbon diffusivity is faster than chromium and the grain boundary diffusivity is faster the lattice results in the precipitation of $M_{23}C_6$ carbides consequently producing chromium depletion zones adjacent to the grain boundary [12]. The formation of $C_{23}C_6$ carbides is susceptible to stress corrosion cracking

along the grain boundaries directly associated with the precipitation of the brittle carbides, where cracking tends to occur. This can result in catastrophic failure of the nozzle due to brittle fracture and loss of coolant. To counteract this effect, low carbon stainless steel (0.015-0.020 wt%) has been developed to prevent sensitization [3]; however, problems are likely to arise when this material is joined to a LAS.

Another concern is the non-uniform microstructure and a discontinuous series of mechanical properties produced in the HAZ by welding. The HAZ is a series of regions affected by the filler metal's high heat output. The coarse grain HAZ (CGHAZ) is the region closest to the fusion boundary in which grain coarsening and softening take place as a result of the high peak temperature [12]. In contrast, in the region adjacent to the CGHAZ, the peak temperature is reduced, resulting in recrystallization and the formation of finer grains, also known as the fine grain HAZ (FGHAZ) [12]. Due to the mismatch in mechanical properties, this region has high residual stress [13] and is a region where premature failure may occur. Moreover, welding is a complex process, i.e., multi-pass welding, which involves the reheating and overlap of HAZs to produce a complex microstructure, resulting in difficulty in inspection and considerable cost in revenue for NPP inspection [14]. To improve the longevity of the NPP components, advancements in design and manufacturing are essential to minimize the defects.

1.3 Powder Metallurgy by Hot Isostatic Pressing

Hot isostatic pressing (HIP) is a near-net shaping (NNS) method to consolidate large components by powder metallurgy (PM) at elevated temperatures and high isostatic pressure to produce an isotropic microstructure with a full density of approximately 95 to 100 percent [15]. It can also be utilized to bond dissimilar metals without welding, as well as aid in the removal of

pores from casted materials and additivity manufactured materials. This procedure employs elevated temperatures typically exceeding 70 percent of the melting temperature and high isostatic pressure ranging from 100 to 200 MPa [16]. Hydrostatically, an inert gas is applied to all sides of the can of steel, which contains the metal powder. The selection of temperature is determined by the material's melting point, as shown in Table 1.

Table 1. General temperature and pressure selection for consolidation using PM-HIP [16].

Material	Melting Point T_m (°C)	Yield Stress at Room Temperature (MPa)	Hipping Temperature (°C)	Hipping Pressure (MPa)
Al and its alloys	660 (Al)	100 to 627	500	100
Al/Al_2O_3	—	—	300	350
Cu and its alloys	1083 (Cu)	60 to 960	800 to 950	100
Be and its alloys	1289 (Be)	240	900	103
Nimonic and superalloys	1453 (Ni)	200 to 1600	1100 to 1280	100 to 140
Hydroxyapatite	—	—	1100	200
Mg/Zn ferrite	—	—	1200	100
TiAl	—	—	900 to 1150	35 to 200
Ti_3Al	—	—	925	200
Ceramic superconductors	—	—	900	100
Steels	1536 (Fe)	500 to 1980*	950 to 1160	100
Ti and its alloys	1670 (Ti)	180 to 1320	920	100
Al_2O_3	2050	5000	1500	100
Al_2O_3/glass	—	—	1400	100
Al_2O_3/TiC	—	—	1935	150
Al_2O_3/ZrO_2	—	—	1500	200
SiC	2837	10,000	1850	200
B_4C	—	—	2000	200
WC/Co	2867	6000	1350	100

*Low-alloy steels (water quenched and tempered).

Since PM-HIP is NNS, the dimensions of the final product are determined by the geometry of the can. By designing the can to resemble the component, both machining time and material scrap are decreased. EPI and Nuclear-ARMC recently demonstrated the capability of PM-HIP by fabricating a pressure vessel head that was 56 percent smaller than its actual size [17]. This work illustrates PM-HIP's ability to manufacture a substantial large component. In addition, Shiokawa et al manufactured a valve body using PM-HIP to reduce machining time by 30 percent [18]. These

works highlighted PM-HIP's ability to reduce cost by minimizing the lead time in processing and manufacturing.

1.4 Factors Influencing the Structural of RPV

Toughness is the most important mechanical requirement for the structural integrity assessment of RPVs [3]. Cooper et al. investigated the effects of higher oxygen concentration and fracture behavior on PM-HIP 316L [19]. He discovered that as the oxygen concentration increased, the inclusions coarsened and the inter-spacing was reduced, resulting in a detrimental fracture toughness of 316L [19]. Duan et al. studied 30CrMnSiNi2A ultra-strength steel consolidated by PM-HIP; he was able to reduce the powder prior boundaries by increasing the processing temperature of HIP; however, this resulted in the coarsening of oxides, which decreased the ultimate tensile strength [20]. Sutton et al. found the toughness of 316L to SA508 by PM-HIP to be significantly diminished due to the formation of intergranular carbides on 316L, while SA508 resulted in carbon depletion from carbon pileup [21]. These defects exist before PM-HIP because the powder was previously exposed to oxygen during storage and handling. Staroulakis et al. developed a transitional material between 316L and SA508 using functionally graded 316L and SA508 by PM-HIP [10]. The author was able to predict the post-HIP microstructure by comparing experimental data and simulations of diffusion.

1.5 Challenges of PM-HIP

Scalability is an issue with the implementation of PM-HIP over traditional forging methods, particularly for large RPV components. First, scaling up necessitates larger and thicker canister walls. The walls of the canister must be sufficiently ductile to deform and should not crack

under high isostatic pressure [22]. In addition, the material inside the canister should be heated and cooled uniformly. Furthermore, uniform heating and cooling become increasingly difficult to maintain control as the thickness grows [22]. In addition, at the end of the PM-HIP process, the canister is mechanically machined to remove the component [22]. To make PM-HIP reusable, a method must be devised for removing the component without causing damage to the canister. Concerns also exist regarding the storage and handling of metal powder particles. Since these particles have a greater surface area, their interaction with air will result in the formation of oxide inclusions on the particle's surface and will have a detrimental effect on the mechanical properties. To prevent the formation of oxides, the powder must be stored under a vacuum in a controlled environment. Gandy et al. studied the room-temperature toughness of A508 after a PM-HIP process in which the powder was stored for six months in both a controlled and uncontrolled environment [17]. He discovered a slight decrease in toughness from 90J to 85J between controlled and uncontrolled environments [17]. Through 800^{o}C vacuum annealing, the toughness was increased to 127J [17]. This study highlighted the significance of residual oxygen reduction and demonstrated that by reducing oxygen, toughness can be enhanced.

Chapter 2: Investigation Methods

2.1. Materials

Powder SA508 (P508) and powder 316L (P316L) were manufactured through inert gas atomization and distributed by Carpenter Powder Products (Bridgeville, PA). P508 possessed a spherical shape and a tap density of 5.3 g/cm^3. The tap density or packing efficiency of PM minimizes voids in the HIP process during densification and is packed efficiently in spherical geometry. P508's particle size ranged from 53 to 500 μm and was predominantly coarse, with 125 to 500 μm accounting for 74% of the size. By inert gas fusion, the average oxygen content was determined to be 103 ppm.

The forged round bars 508 (B508) and bar 316L (B316L) were manufactured by Scot Forge (Spring Grove, IL) and Valbruna (Fort Wayne, IN), respectively. SA508 ingots were melted using an electric furnace ladle in a refined vacuum to produce an outer ring with the following dimensions: inner diameter: 49 inches, outer diameter: 39 inches, and length: 12 inches. The outer ring was heat treated at Ellwood Quality Steels Company at normalization temperature (950^{o}C for 5.25hrs), followed by water quenching and tempering (650^{o}C for 8.25h) then machined by Electric Power Research Institute (EPRI) to a round bar measuring 5 inches in diameter and 2 inches in length. The average oxygen content of B508 was found to be 63 ppm by inert gas fusion. Likewise, B316L was forged to the same dimensions as B508. It is noted that B316L was not heat treated after the forged condition was completed. Table 2. lists the nominal chemical compositions of P508/P316L and B508/B316L.

Table 2. Chemical composition of SA508 and 316L SS.

	Composition (wt%)										
Element	C	Ni	Cr	Fe	Mn	Mo	N	O	P	S	Si
P508	0.17	0.84	0.11	Bal.	1.19	0.52	0.03	0.009	0.012	0.004	0.31
B508	0.2	0.77	0.39	Bal.	0.72	0.64	-	-	-	0.021	0.26
P316L	0.014	12.22	18.13	Bal.	1.40	2.35	-	-	0.006	0.011	0.77
B316L	0.015	10.22	16.72	Bal.	1.78	2.09	0.08	-	0.022	0.023	0.67

2.2. PM-HIP and post-heat treatment

Before the fabrication of the dissimilar metal joint by PM-HIP, B508 was inserted into the canister followed by P508 then the canister was sealed and processed with vacuum annealing to remove the residual oxygen from P508. It is noted that P316L-B508 was not vacuum annealed. The canister was sealed and placed inside of the HIP furnace (KittyHawk) and heat-treated at 1163^{o}C for 3h under 103 MPa isostatic pressure and allowed to slowly air-cool inside the HIP chamber until room temperature was reached. The powder and round bar were compacted at elevated temperatures and pressure in the HIPper to achieve strong bonding between materials and densification. All the dissimilar metal joints received the same processing conditions. From PM-HIP, two billet designs were created: 1) P508 to B316L and 2) P316L to B508. Figure 3 depicts the completion of powder-to-round bar consolidation for both joint designs. In both instances, the powder samples shrank as a result of the elevated temperature and high pressure which led to densification and the consequent elimination of pores.

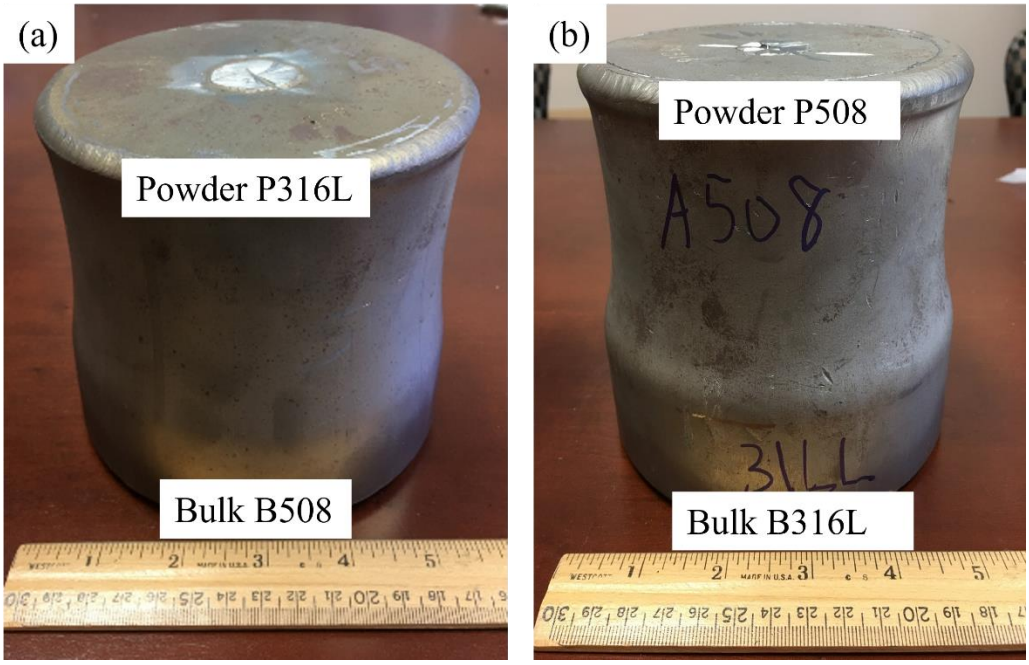

Figure 3. The dissimilar metal joint billet after PM-HIP of powder to bulk material a) P316L to B508, b) P508 to B316L.

Thin rectangular plates were cut from the billets using wire electrical discharge machining (EDM). Table 3. highlights the heat-treatment conditions used for this study. It is noted that the as-received condition was not heat-treated after fabrication. All heat treatments were conducted in the Mellen box furnace. Once the desired temperature was attained, the samples were loaded into the furnace chamber and the hold time was measured upon reaching the proper temperature. The conditions for solution annealing (SA) and normalization (N) were water quenched (WQ), while tempering (T) was air-cooled (AC) outside the furnace. In addition, the tempering condition was tested a 650^{o}C and 550^{o}C for a duration of 4h each after SA and N.

Table 3. Summary of materials and heat-treatments

Material	Heat-treatment
P316L-B508	As-received
P508-B316L	
P316-B508	Solution annealed (1065^{o}C-2h+WQ)
P508-B316L	Tempered (650^{o}C-4h +AC)
Pure P316L	Solution annealed (1065^{o}C-2h+WQ)
Pure P508	Normalized (900 ^{o}C-2h+WQ)
P508-B316L	Tempered (650^{o}C-4h+AC)
P316L-B508	Solution annealed (1065^{o}C-2h+WQ)
	Normalized (900 ^{o}C-2h+WQ)
	Tempered (550^{o}C-4h+AC)
	Solution annealed (1065^{o}C-2h+WQ)

2.3. Mechanical testing

2.3.1 Tensile test

The PM-HIP specimens P316L-B508 and P508-B316L were heat-treated to the SA+N+T(650^{o}C) condition followed, and then wire EDM was utilized to produce cylindrical tensile bars following ASTM E8M specimen type 4 for specimens with a gauge length of five times the diameter. Figure 4. illustrates the geometry of the tensile bar. The length, gage length, width, and thickness were 76.2 mm, 31.75 mm, 12.7 mm, and 6.35 mm, respectively. At the center

of the tensile bar, the interface is shown. For machining, the center needed to be the precise region where the two dissimilar metals met.

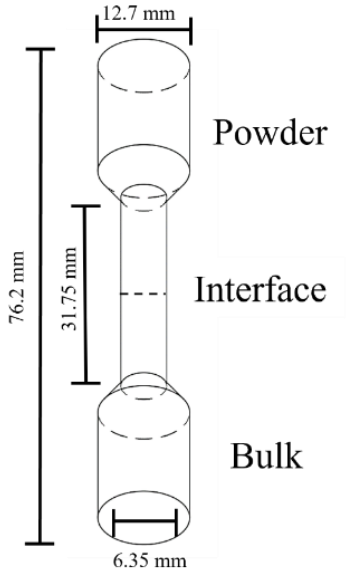

Figure 4. Schematic of the tensile specimen.

Tensile tests were performed at a strain rate of 0.002/s with the Instron 880 hydraulic tester and the strain upon testing was measured by digital image correlation (DIC) using Correlation Solutions VIC-3D 9 setup. Figure 5. shows a general layout of the VIC-3D 9 setup for the tensile test. To begin, the cylindrical tensile bars were polished with 220 grits to remove the EDM marks and to produce a clean surface followed by the application of a black base coat of spray paint that produced an isotropic speckle pattern. After the specimen had dried, it was mounted in the tensile tester. The DIC system was set by mounting two cameras (Basler acA2440) with their respective compact lenses (Schneider Compact 8 mm f/1.4) onto a tripod where the camera was at an angle between 15 to 45 degrees. The compact lens had a working distance of 1:1, thus the tripod was placed close to the tensile tester. Next, two light sources were placed in front of the specimen to

achieve sharp contrast, and the image-capturing software, VIC-Snap, was calibrated. For the calibration, minor adjustments were made to the light source, camera angle, and working distance to minimize noise, and then 20 images were taken using a 4mm-spaced calibration plate to calibrate the software. Upon completion of the tensile test, the stress data from the tensile test and the strain data from DIC were combined to create a stress-strain plot. This test was performed twice at SA+N+T(650^{o}C) P316L-B508 and P508-B316L.

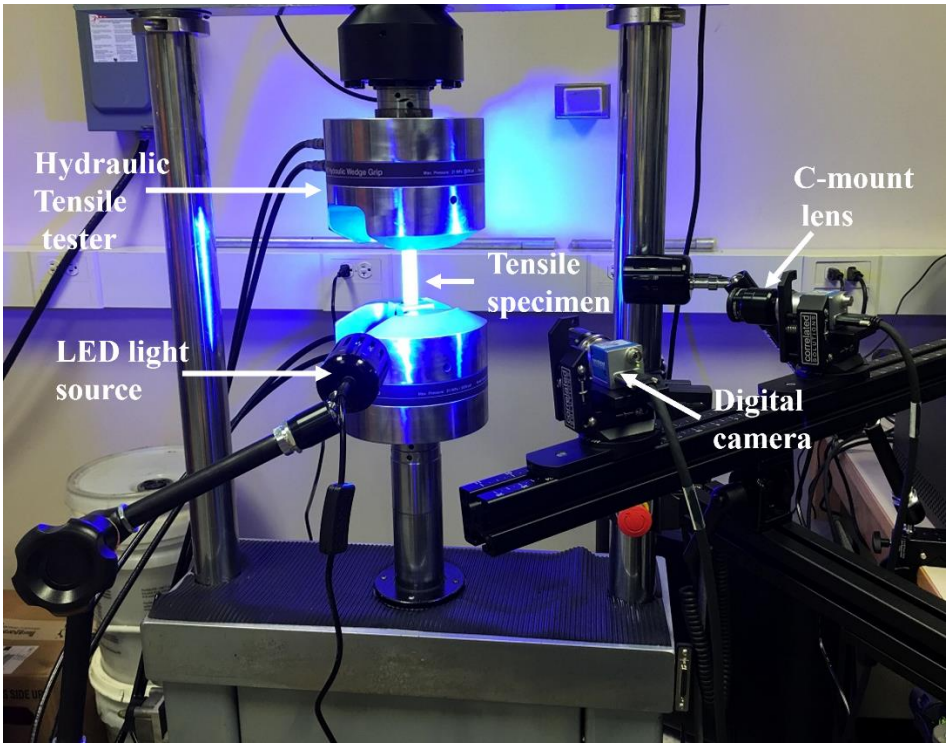

Figure 5. Schematic of the DIC setup used for tensile test.

2.3.2 Charpy impact test

The Charpy v-notch bars were machined by wire EDM following ASTM E23 as shown in figure 6. Optical microscopy was used to ensure that the v-notch on each bar was positioned directly on the dissimilar metal's interface. The v-notch angle and dimension of the bar were measured to be within the ASTM E23 tolerance range. The impact test was conducted at ambient

temperatures using the Tinius Olsen pendulum impact tester (maximum energy 264 ft-lb at impact velocities of 16.87 ft/sec). The tester's base was calibrated to be leveled to ensure the proper distribution of force. The sample was positioned and aligned so that the v-notch faced away from the pendulum in the specimen holder. On average, two to four tests were conducted for every Charpy impact condition.

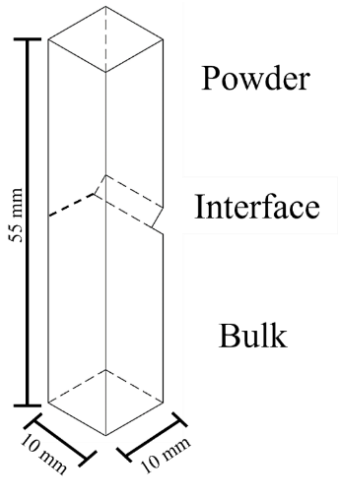

Figure 6. Schematic of Charpy v-notch impact bar.

2.3.3 Vickers hardness

The Leco DM-400 hardness tester with a Vickers diamond tip was used to measure the microhardness of the finely polished dissimilar metal joint. Optical microscopy was used to ensure that there were no scratches on the sample's surface. On each specimen, a load of 0.1 N, an interspacing distance of 150 μm, and a dwell time of 15s were applied for all measurements. A series of 15 indents were made perpendicularly to the interface and repeated in parallel for an average of three times, yielding 45 indentations per specimen. P316L-B508 and P508-B316L were tested for microhardness under as-received and SA+N+T(650^{o}C) conditions.

2.3.4 Nanoindentation mapping

The iMicro nanoindenter (KLA instrument) with a Berkovich diamond tip with blitz method was used to create the nanoindentation mapping consisting of 100 indents (200 x 200 array) per sample. The load was maintained at 20 mN while the depth varied between 400 to 700 μm; optical microscopy revealed good resolution. In addition, the interspacing between each indentation was set to 20 μm, which was determined to be the optimal distance to prevent plastic deformation from the overlapping indents. Nano-indentation was performed near the interface between the joints to understand the cause of the high hardness at the interface and to examine the extent of hardness. This test was conducted on P316L-B508 and P508-B316L at as-received and SA+N+T(650^{o}C) conditions.

2.4. Sensitization

To prepare the samples for sensitization, steel wire was spot-welded to the back of the sample's interface, followed by cold mounting. The mixture used was composed of Epofix at 25 wt% resin and 3 wt% hardener followed by a 24 h cure time. The area of the samples was then measured to determine the required current density for sensitization followed by fine polishing of the sample's surface, which will be discussed in the next section. For the sensitization test, the electrolyte containing 10 % ammonium persulfate and balanced with water was placed in a glass beaker. As for the electrolyte's cathode, a stainless-steel mesh basket was used and the anode was the specimen's back wire, which functioned as a contact point to transfer current uniformly throughout the sample. The direct current was controlled with a voltmeter and evaluated at 1 A/mm^2 for 10 mins under ASTM A262. The tested samples were P316L-B508 as-received, SA, SA+T, SA+N+T(650^{o}C), and SA+N+T(550^{o}C) conditions.

Lastly, optical images of all the previously mentioned conditions were taken for the P316L side and the sensitization distances were measured for an average of 10 times by using ImageJ. The measurements were taken perpendicularly from the interface of P316L. Furthermore, the sensitized grain boundary widths were measured at a distance of 300 μm away from the interface an average of 20 measurements were conducted along the direction of the interface of the P316L side using ImageJ. Figure 7 illustrates the method of measuring the sensitized boundary widths. A plot of sensitization distance as a function of grain boundary width of all the heat-treated conditions was created.

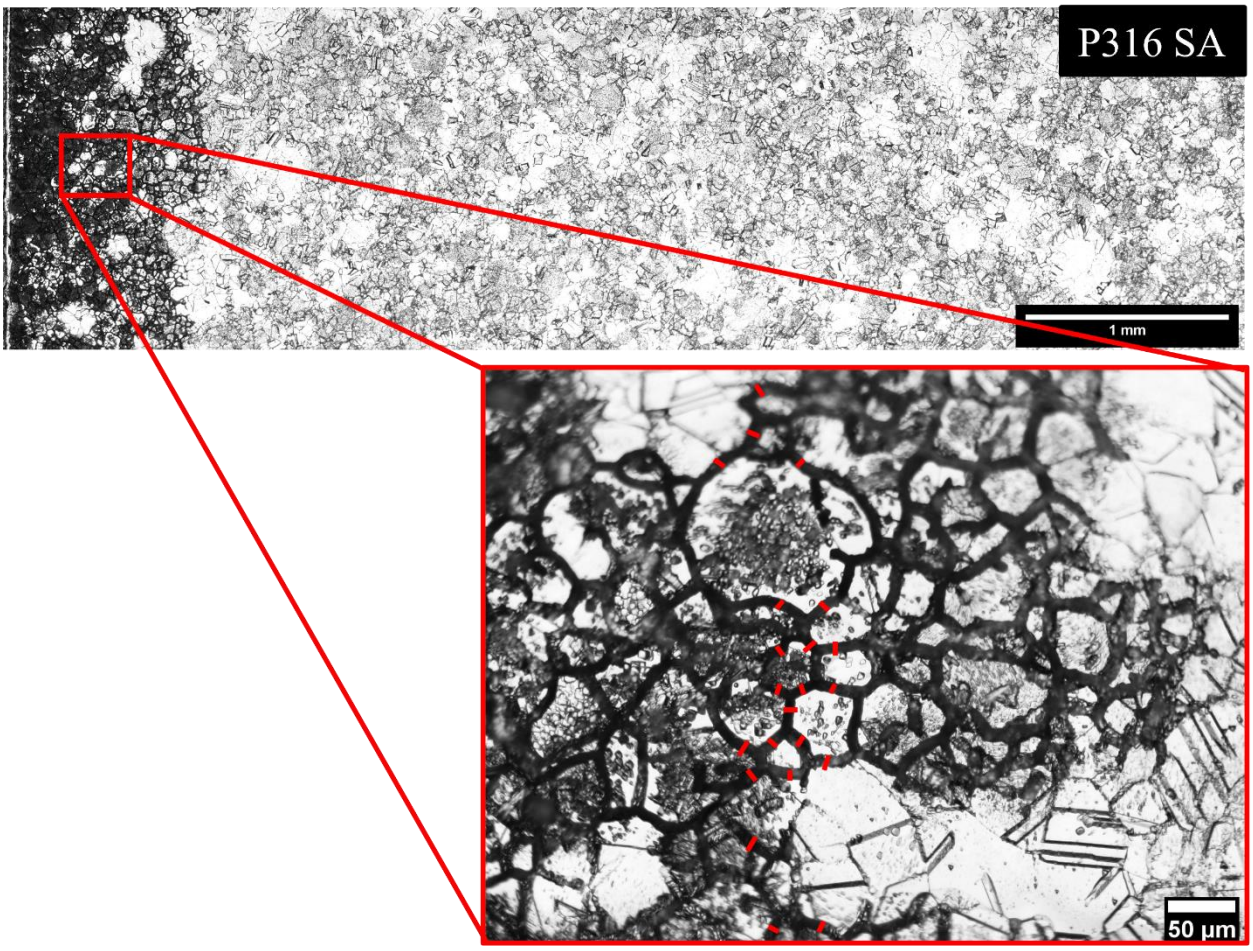

Figure 7. Example of the sensitized sample SA P316L side of B508. The inset demonstrates the method of measuring the sensitized grain boundary widths.

2.5. Microstructural characterization

To reveal the microstructure, the specimens were polished using the Struers TegraPol-15 auto polishers beginning with 200 grits and increasing to higher grits with 0.9, 0.3, and 0.05 μm suspension. The samples were cleaned with water and dried with nitrogen gas after each step to prevent contamination. SA508 was etched for 30 sec to 2 mins with Viella's reagent containing 1 gram of picric acid, 5 ml of hydrochloric acid, and 100 ml of ethanol. 316L was etched with 10% oxalic acid balanced with water at 5V for 45 sec to 3 mins. The etched samples were washed with water and dried with nitrogen gas to eliminate any lingering chemicals. The microstructure was examined by using the Olympus BX51 optical microscope under magnification between 5 and 50.

To characterize the carbides and the fractography the scanning electron microscope (SEM) by JEOL JSM 7000 F with an Energy Dispersive X-ray Spectroscopy (EDS) detector by Oxford Instruments was used. Additional polishing was necessary to achieve a surface without scratches. The vibratory polisher (Buehlers) utilized a fine polishing cloth with 0.04 μm colloidal silica suspension for 45 minutes at 10 percent amplitude. Due to the low corrosion resistance of SA508, the duration of the final polishing was shortened to prevent corrosion. To remove, any suspension residue and corrosion the samples were placed in ultrasonication in an acetone bath for 15 mins. The characterization of oxides and carbides was done by SEM with voltages of 20kV and 10kV, respectively. EDS was used to measure the intensity profile of Cr, Ni, and Fe on the interface between dissimilar metal joints. The counts were converted to weight percent using a linear fit, with the assumption that the weight percent of Cr and Ni in SA508 was set at 0 wt%. This assumption was accurate because the initial Cr and Ni concentrations in SA508 were 0.39 wt% Cr and 0.77 wt% Ni. Fe was subtracted from the converted Cr and Ni to determine the Fe percentage by weight.

2.6. Simulation of the diffusion couple

Thermodynamic and kinetics modeling of dissimilar metal joints by simulation is a powerful tool for process optimization before experimental testing. Pandat (CompuTherm) incorporates the PanDiffusion module a thermodynamic and equilibrium modeling software based on the Calculation of Phase Diagram (CALPHAD). This software relies on thermodynamic equilibrium to calculate the kinetics, it is incapable of calculating non-equilibrium conditions; consequently, rapid or continuous cooling cannot be included in the modeling.

PanDiffusion module computes the one-dimensional diffusion of two or more dissimilar metals as molar phase fractions in equilibrium as a function of composition, temperature, and distance. The diffusion couple simulations were performed using this module in combination with the Fe database to calculate Fe-rich alloys. In this study, 316L was joined directly to SA508 by simulation. The parameters were set to automatic flux interface, mesh size at 300, uniform distribution, planar geometry, a total distance of 8000 μm, and the sigma phase was suspended. In addition, the boundary conditions were with fixed compositions, with the upper and lower limits set to 0.014 wt% C and 0.2 wt% C, respectively. Table 4. illustrates the chemical composition used for the simulation. These conditions were fixed for all the simulated results, except for the thermal history. These conditions were fixed for all the simulated results, except for the thermal history. Four heat treatments were selected for this experiment: 1) as-received (1163^{o}C-3h), 2) AR + SA (1065^{o}C-2h), 3) AR + SA + N (900^{o}C-2h) + T (650^{o}C), and 4) AR+SA+N+T(550^{o}C). Table 5. depicts a summary of the thermal history used for the simulation.

Table 4. 316L and SA508 compositions used in PanDiffusion.

	Composition (wt%)						
	C	**Cr**	**Ni**	**Fe**	**Mn**	**Mo**	**Si**
316L	0.015	16.72	10.22	Bal.	1.78	2.09	0.67
SA508	0.20	0.39	0.77	Bal.	0.72	0.64	0.26

Table 5. Simulated diffusion couples using Pandat's PanDiffusion module.

Diffusion Simulation	**Temperature**			
As-received	1163ºC			
Solution annealed	1163 ºC	1065 ºC		
Solution annealed, normalized, tempered	1163 ºC	1065 ºC	900 ºC	650 ºC
Solution annealed, normalized, tempered	1163 ºC	1065 ºC	900 ºC	550 ºC
	Dwell time			
	3 hour	2 hours	2 hours	4 hours

Additionally, modeling using PanDiffusion with the Ni-database was utilized to create two alternative joint designs in effects to reduce the formation of $M_{23}C_6$ carbides. The two designs were 1) SA508 to 600M to 316L and 2) SA508 to 82 to 316L. The compositions of C, Cr, Fe, Ni, and Nb were selected for the simulation as shown in Table 6. The selected thermal history was set to SA+N+T(650ºC). In addition, the parameters used were the same as the simulation based on 316L to SA508 except for the mesh size (200), thickness (15,000 μm), upper boundary (0.20 wt% C), and lower boundary (0.015 wt% C).

Table 6. 600M and 82 compositions used in PanDiffusion.

Composition (wt%)					
	C	Cr	Fe	Ni	Nb
600M	0.02	15.6	8.1	Bal	1.9
82	0.04	19.9	0	Bal	2.5

Lastly, a functionally graded composition composed of 316L to SA508 was simulated with PanDiffusion with the Fe-Database at intervals of 10 wt% to 90 wt% 316L balanced with SA508. The mixed composition is shown in Table 7, where the elements C, Cr, Fe, Mn, Mo, Ni, and Si were selected. For the calculations, the mixed alloy was first bonded to 316L, then the mixed alloy was bonded to SA508. Thus, there was a total of 18 different designs at 10% intervals of 316L. In addition, the thermal history was set to SA+N+T(650^{o}C). The sigma phase was suspended, and the mesh size was set to 400 μm. Furthermore, only the maximum carbon peaks were obtained to determine the best composition to use for functionally graded composition.

Table 7. Graded 316L with SA508 composition used in PanDiffusion.

Composition (wt%)							
Mixed alloy	C	Cr	Fe	Mn	Mo	Ni	Si
10% 316L+90% 508	0.182	2.02	Bal.	0.83	0.79	1.72	0.30
20%316L+80% 508	0.163	3.66	Bal.	0.93	0.93	2.66	0.34
30%316L+70% 508	0.145	5.29	Bal.	1.04	1.08	3.61	0.38
40%316L+60% 508	0.126	6.92	Bal.	1.14	1.22	4.55	0.42
50%316L+50% 508	0.108	8.56	Bal.	1.25	1.37	5.50	0.47
60%316L+40% 508	0.089	10.19	Bal.	1.36	1.51	6.44	0.51
70%316L+30% 508	0.071	11.82	Bal.	1.46	1.66	7.39	0.55
80%316L+20% 508	0.052	13.45	Bal.	1.57	1.80	8.33	0.59
90%316L+10% 508	0.034	15.09	Bal.	1.67	1.95	9.28	0.63

Chapter 4: Results

4.1. Microstructure under different heat treatments

Figure 8 illustrates the microstructural evolution from the as-received condition to SA+T to SA+N+T(650^{o}C). The dissimilar metals P508 and P316L were characterized with an emphasis placed near the interface of both materials. The as-received condition of P508 was observed to be composed of a high-volume fraction of α-ferrite, a layer of bainite at the interface, and small-volume fractions of bainite throughout P508. Polygonal ferrites were formed as a result of continuous cooling due to the air-cooling nature of the PM-HIP process [23]. The formation of bainite along the interface was caused by the abrupt change in carbon chemical potential since the transform kinetics of bainite is dependent on the diffusion of carbon [23]. The microstructure of bainite is composed of ferritic sheaves with plates with each sheaf separated by cementite [24] and its good toughness is due to the high angle boundaries (>15^{o}) that effectively prevent crack propagation [25]. For structural components in NPPS, it is desirable to have a component with high toughness since in the likelihood of a defect and under deformation it prevents premature failure from occurring.

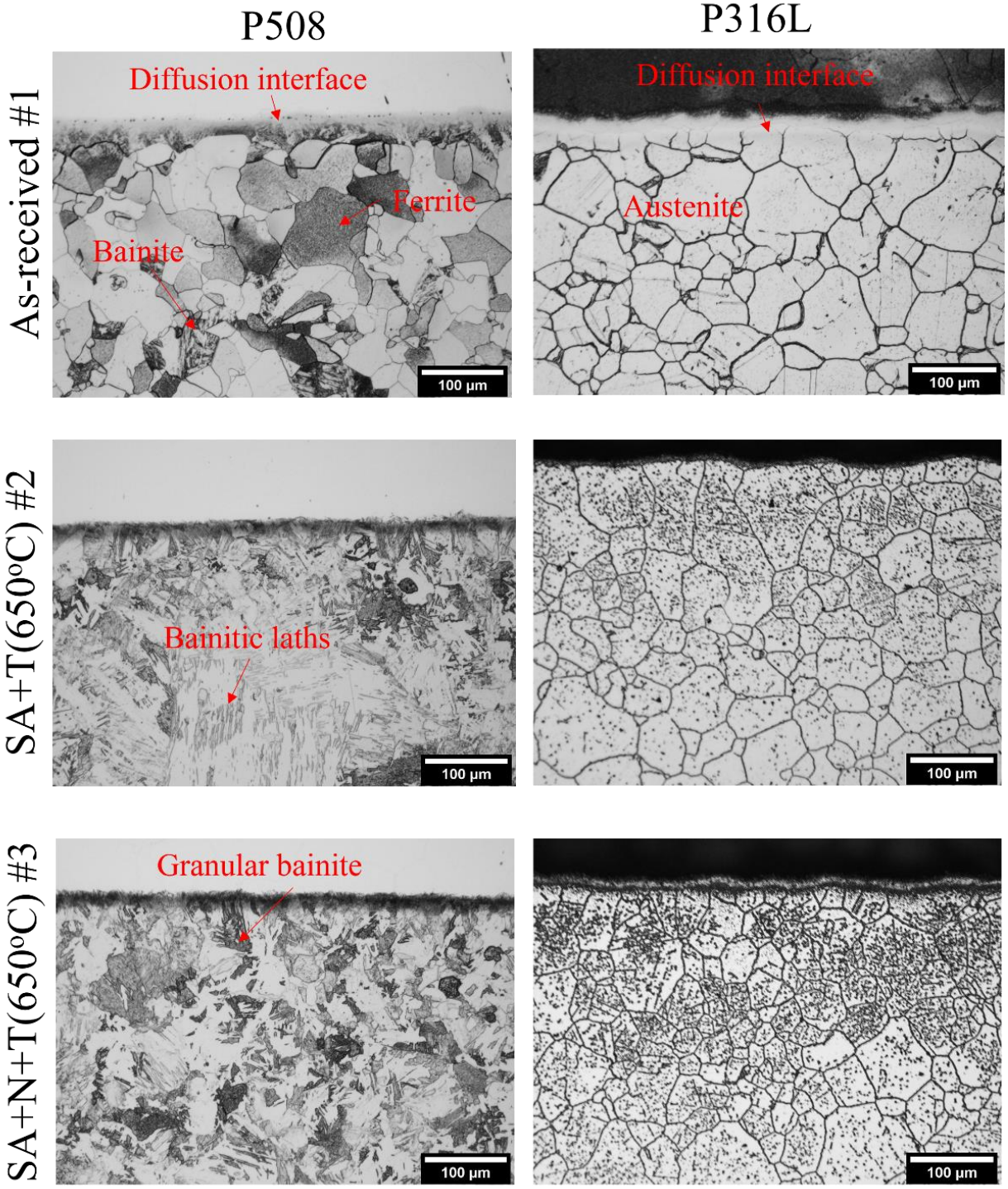

Figure 8. Optical images of etched microstructure for P508 and P316L at as-received, SA+T, SA+N+T(650°C) conditions.

Solution annealing and tempering were performed to enhance the volume fraction of the bainitic microstructure. Solution annealing was used to create a single phase and dissolve any intermetallic phases, i.e. carbides. In contrast, tempering was performed to reduce brittleness and increase grain size, thereby enhancing ductility and toughness. At this condition, P508 was characterized by coarse, nearly parallel laths of bainite and granular bainite. Granular or irregularly shaped bainite contained retained austenite islands of a martensite and austenite mixture [24], where the toughness is proportional to the amount of martensite phase. By performing normalization between solution annealing and tempering, microstructures composed of granular bainite were produced. Compared to solution anneal and tempering, the microstructure exhibited considerable grain refinement.

In the as-received condition of P316L, it was observed to have equiaxed austenitic grains. The same heat-treatment conditions were applied to P316L and did not change the phase since the stability of austenite was caused by the high Ni content. Similarly, the heat treatment of SA+N+T compared to SA+T resulted in grain refinement. For this study, SA+N+T was the chosen heat treatment due to the improvement in strength and ductility to enhance the impact toughness.

4.2. Dissimilar metal interface

Figure 9. shows the SEM micrograph of the B316L-P508 and B508-P316L at as-received and SA+N+T conditions. After nano-indentation was performed, micrographs were taken, and P508 was lightly etched before characterization. An EDS line scan was performed on both as-received B316L-P508 and B508-P316L to examine the abrupt change in the compositional profile of Fe, Cr, and Ni at the interface. Carbon was excluded from the line scan because, as an institutional element, it could not be detected accurately by EDS. According to this analysis, Cr

and Ni diffused from B316L to P508, whereas Fe migrated from P508 to B316L. Differences in initial composition were responsible for the diffusion. Since PM-HIP operates at elevated temperatures, the difference in chemical potential acted as a thermodynamic driving force for the diffusion of substitutional atoms from high concentration to low concentration. Similarly, B508-P316L at the as-received condition exhibited the same compositional trend.

For the as-received P508-B316L coarsen spherical oxides inclusions rich in Mn and Si were identified by EDS point identification at the interface of P508-B316L. The dimensional diameter was measured by ImageJ to be 2.1 μm. In contrast, as-received P316L-B508 did not exhibit oxide precipitates at the interface. This implied that the formation of the oxides was due to P508 and not P316L. It is believed that the presence of oxides is the result of improper powder shipping and handling, with the powder's high surface area trapping oxygen atoms exposed to the environment. Upon, PM-HIPing the inclusions formed around the prior particle boundaries (PPB). After the elevated temperature removed the PPB from PM-HIP, the oxides became coarser due to the elevated temperature and the Ostwald ripening effect [20]. In addition, the as-received condition insets reveal a fine concentration of carbides with a size of 0.1 μm embedded in the grain at the interface of P508 and B508. These carbides originated from the PM-HIPing's gradual cooling.

When P508-B316L was subjected to SA+N+T, the oxides at the interface remained. In the inset of P508-B316L, cementite (Fe_3C) was identified at the interface by EDS point identification with a measured length and width of 0.6 μm and 0.15 μm, respectively. The observed shape of cementite as elongated spheres surrounded by a ferrite matrix is believed to be the result of a prolonged tempering condition. Reduced hardness is a characteristic of spherodized cementite, which can reduce interfacial brittleness [26]. In contrast, heat-treated P316L-B508 at the inset

exhibited the precipitation of globular carbides along the grain boundary and within the grain interface. The formation of carbides along the carbide is detrimental to the toughness since the brittle carbides provide an easy path for the crack to propagate.

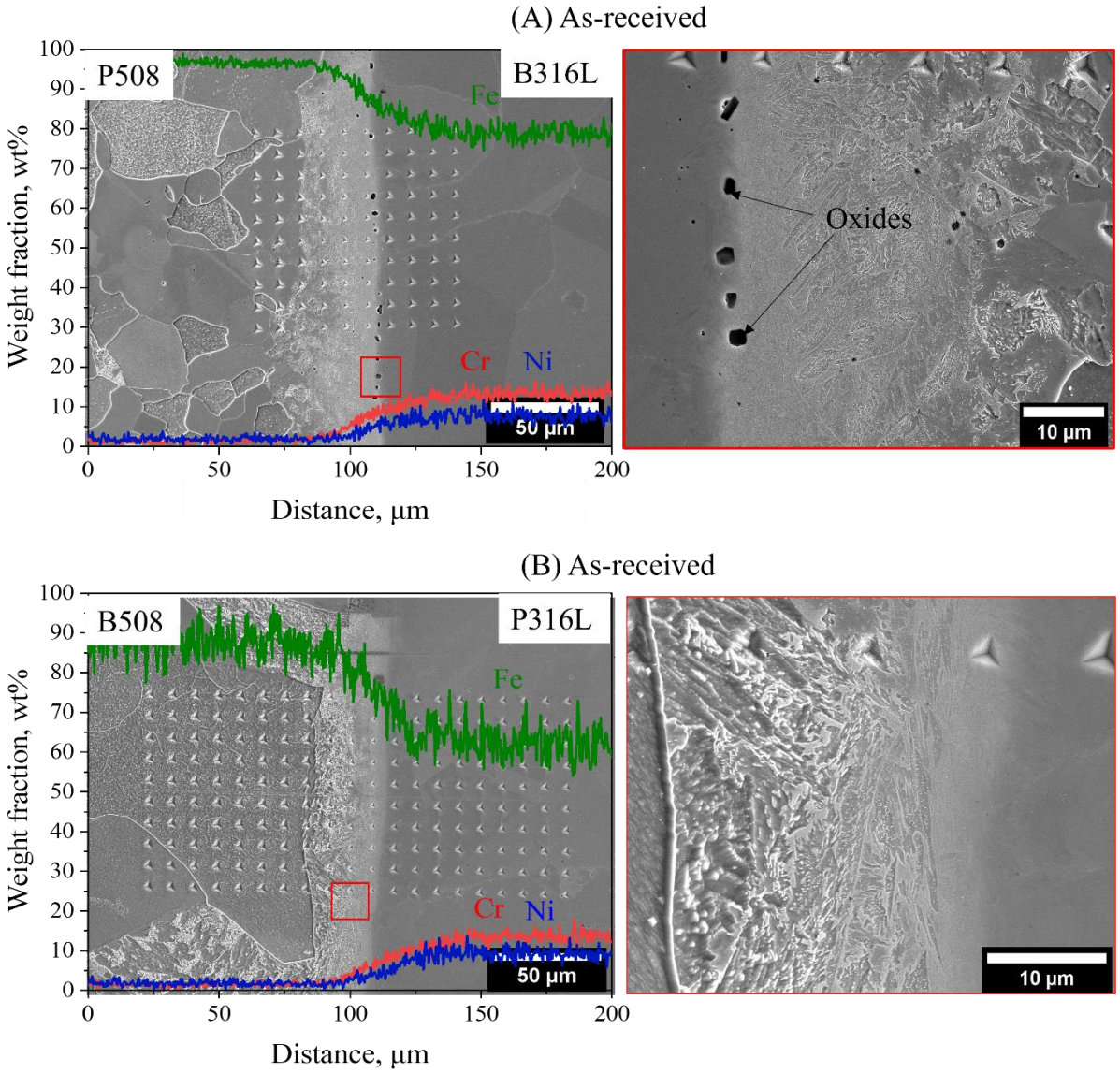

(C) Solution annealed; normalized; tempered (650°C)

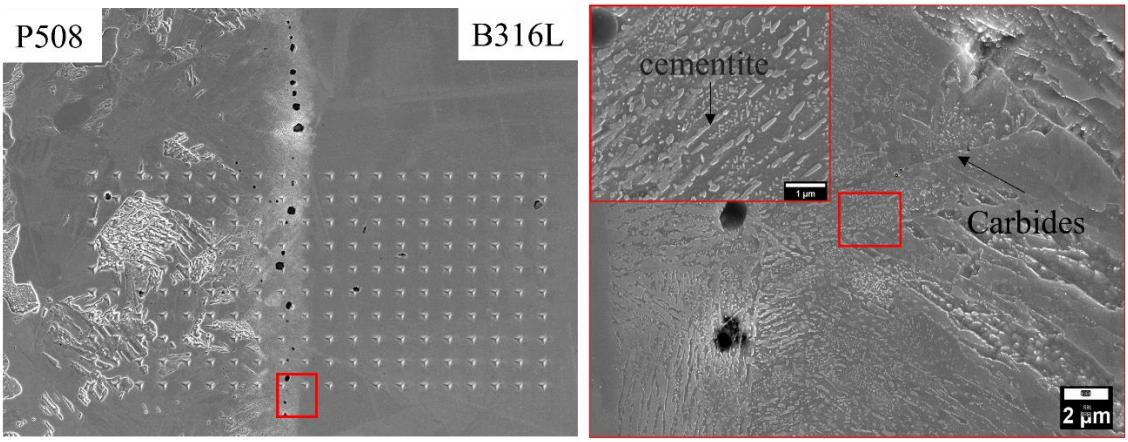

(D) Solution annealed; normalized; tempered (650°C)

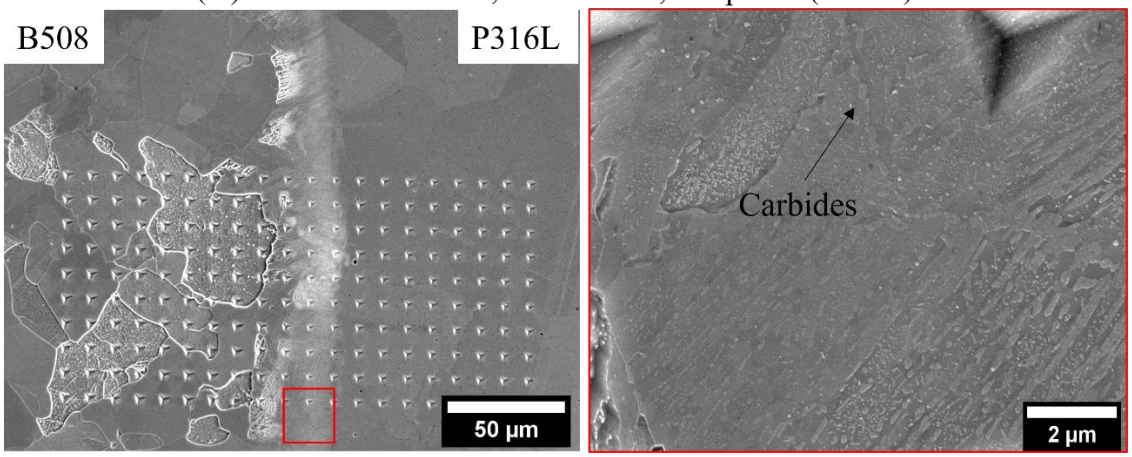

Figure 9. SEM images of the etched surface for as-received a) P316L-B508, b) P508-B316L and SA+N+T c) B316L-P508 d) B508-P316L. EDS line scan was performed for both as-received P316L-B508 and P508-B316L.

4.3. Tensile properties

Figure 10. shows the engineering stress-strain curves of SA+N+T P316L-B508 and P508-B316L. The ultimate tensile strengths (UTS) for P316L-B508 and P508-B316L were 612 MPa and 596.5 MPa, respectively. The tensile data showed that both materials had similar UTS. The

yield strength for P316L-B508 and P508-B316L were 346 MPa and 284 MPa, respectively. P316L-B508 displayed a higher yield strength, hence it can handle more load before plastic deformation. The data shows that the yield strength was satisfactory in meeting the ASME code. Figure 10b. and c shows the strain rate for 316L and SA508. The strain for P316L and B316L was around 0.7 and 0.9, respectively. Whereas the strain rate of P508 and B508 remained constant strain, hence the SA508 did not yield. Thus, B316L-P508 exhibited higher elongation after the tensile test compared to B508-P316L. Therefore, it was concluded that the interface was sufficiently strong enough to resist deformation. Table 8. shows a summary of the tensile results.

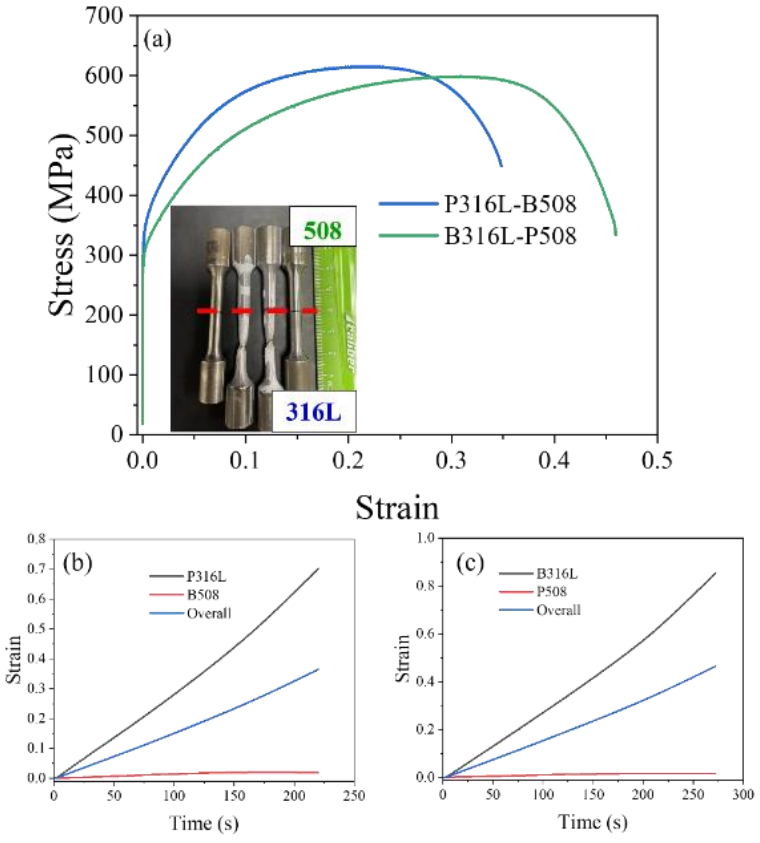

Figure 10. Tensile test results after heat treatment at SA+N+T(650^{o}C) condition for (a) P508-B316L and P316L-B508; strain rate results for (b) P316L-B508; (c) P508-B316L.

Table 8. Summary of tensile results

	YS (MPa)	UTS (MPa)
P316L-B508	346.5±2	612±2.8
B316L-P508	284±4.96	596.5±2.1

Figure 11. displays the SEM fractography of the broken tensile bar's surface for P316L and B316L. Both P316L and B316L exhibited ductile fractures characterized by dimples. The inset of P316L displayed fine inclusion embedded in the cavities of the dimples at a diameter of 0.4 μm. These inclusions were believed to be oxides and were identified by EDS point identification in the fractography of the broken Charpy impact bars interface, which will be discussed in the later chapters. The display of oxides located on P316L revealed that the powder 316L particles were caused by the high surface area of the particle's high tendency for oxygen entrapment for the same reason as P508 as previously discussed. Cooper et al PM-HIP 316L with an oxygen concentration of 100 ppm and found that the average pore radius was between 0.1 to 0.5 μm with an area fraction of oxides between 0.12 and 0.22 % [27]. He concluded that the higher volume fraction of oxides resulted in a reduction in fracture toughness when compared to forged 316L with no oxides. Cooper's study showed evidence that P316L oxides may contribute to a lower toughness for P316L-B508.

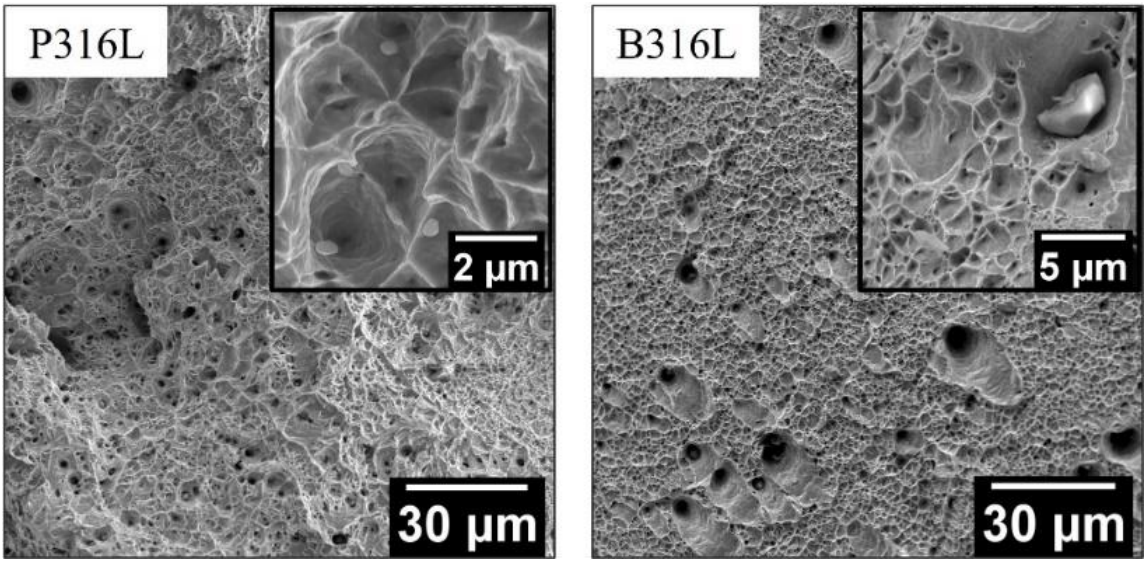

Figure 11. SEM images of fracture surface after tensile test at room temperature for heat-treated conditions P316L and B316L of dissimilar metal joints.

In B316L several pores were observed these pores were an indirect effect of the large oxides observed in P508 previously shown in figure 11. As the tensile test proceeded in elongating the specimen the oxides were dislodged leaving a void behind at B316L [27]. In addition, large irregular shape inclusion with a length and width of 4.5 µm and 0.4 µm, respectively, were found on the inset.

4.4. Charpy impact properties

Figure 12 shows the comparison of different heat-treated conditions' influence on the energy absorption for P508-B316L, P316L-B508, pure P316L, and pure P508. The toughness was evaluated by the Charpy impact test at room temperature. Solution annealed + normalization + tempering (650^{o}C) was performed on pure P316L, pure P508, P316L-B508, and P508-B316L and the toughness values were the following: 169J, 69J, 35J, and 23J, respectively. As expected, pure

P316L exhibited the highest toughness followed by pure P508, since these materials did not have a dissimilar interface. However, the recorded toughness values were significantly lower than expected. Sutton et al found the toughness at room temperature of B316L and B508 to be 206 J and 177 J, respectively [21]. Although, his heat-treatment conditions were different the toughness values should have been similar since the heat-treatment conditions were designed to improve strength and ductility. Figure 13. showed the optical image of the fractured surface and SEM images of the fracture morphology after the Charpy impact test for pure 316L, pure P508, P316L-B508, and P508-B316L at solution annealed + normalized + tempering condition. Pure P316L and pure 508 exhibited ductile failure and revealed oxides located across the fractured surface with particle sizes of 0.8μm and 0.4μm, respectively. The reduction in toughness was caused by the high oxygen concentrations leading to a high-volume fraction of oxides for both materials.

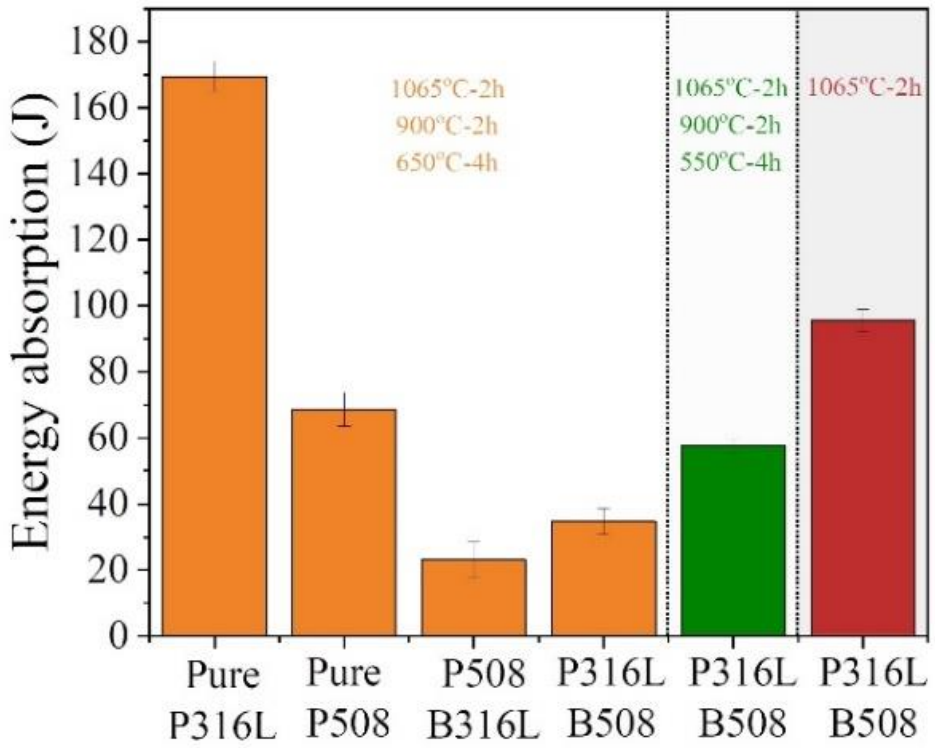

Figure 12. Charpy impact toughness at room temperature for pure 316L, pure P508, and P508-B316L all heat-treated at 1065^{o}C-2h, 900^{o}C, and 650^{o}C-4h; P316L-B508 at 1065^{o}C-2h, 900^{o}C-2h, and 550^{o}C; P316L-B508 at 1065^{o}C-2h.

At the same condition, P508-B316L exhibited the lowest toughness followed by P316L-B508 shown in figure 12. Both materials displayed brittle failure by intergranular fracture. In the inset found in figure 13 coarsen inclusions with a particle size range of 1 to 3 μm were observed to be located on the interface of P508-B316L. The high initial oxygen concentration of P508 at 103 ppm, led to the precipitation of coarsening oxides. Since these inclusions were located on the interface it resulted in toughness depreciation. The formation of oxides acted as void nucleation sites resulting in easy crack propagation upon the Charpy impact test. In comparison, the SEM image of P316L-B508 did not display any inclusions. It is noted that the oxides did exist at the interface, however, due to the low magnification of the image taken the oxides were not revealed. In figure 11, it was established that fine oxides were dispersion throughout the interface of the P316L. Thus, it showed an improvement in toughness of 35J compared to 23J from P508-B316L. Due to the detrimental effects of oxides P508-B316L was eliminated from the study and the emphasis on toughness improvement was placed on P316L-B508.

P316L-B508 at solution annealed + normalization + tempering (550^{o}C) and solution annealed displayed toughness values of 58 J and 96 J, respectively. The toughness was found to be improved by reducing the tempering temperature from 650^{o}C to 550^{o}C. However, the data was found to be concerning, since the solution annealing condition resulted in the highest toughness of 96 J. This phenomenon was uncommon since, solution annealing followed by quenching creates a

harder phase, hence the toughness should be reduced. This suggested that other mechanisms were responsible for the low toughness of P316L-B508.

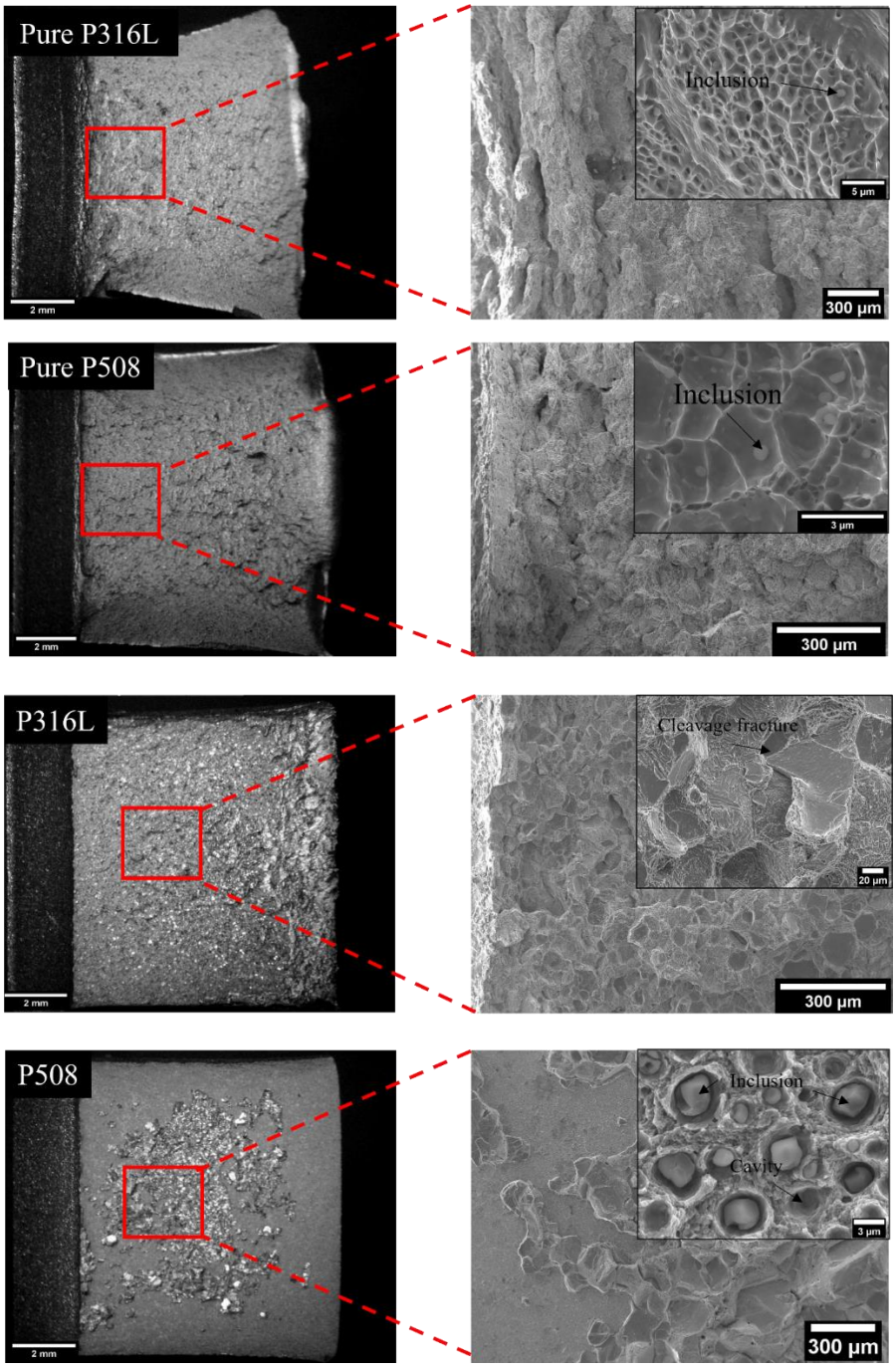

Figure 13. Optical images of Charpy fracture surfaces after testing at ambient temperature for pure 316L, pure P508, P508-B316L, and P316L-B508; heat-treated at 1065^{o}C-2h, 900^{o}C, and 650^{o}C-4h. The inset shows SEM micrographs of the fractured surface.

4.5. Micro- and nano-hardness profile across the interface

4.5.1. As-received

Figure 14(a-b). shows the micro-hardness and nano-indentation profiles of as-received P508-B316L and P316L-B508. As received P316L-B508 and P508-B316L, both exhibited non-uniform microhardness distribution across SA508. The hardness data depicted that the non-uniform microhardness was caused by the microstructure. This is shown by the dual structure of SA508 possessing soft ferrite and hard bainite. P508 and B508 microhardness ranged from 143-281 HV and 142-307 HV, respectively. In addition, the microstructure of 316L's austenite phase remained unchanged, resulting in consistent microhardness. The microhardness ranged between 170-210 HV and 155-191 HV for P316L and B316L, respectively

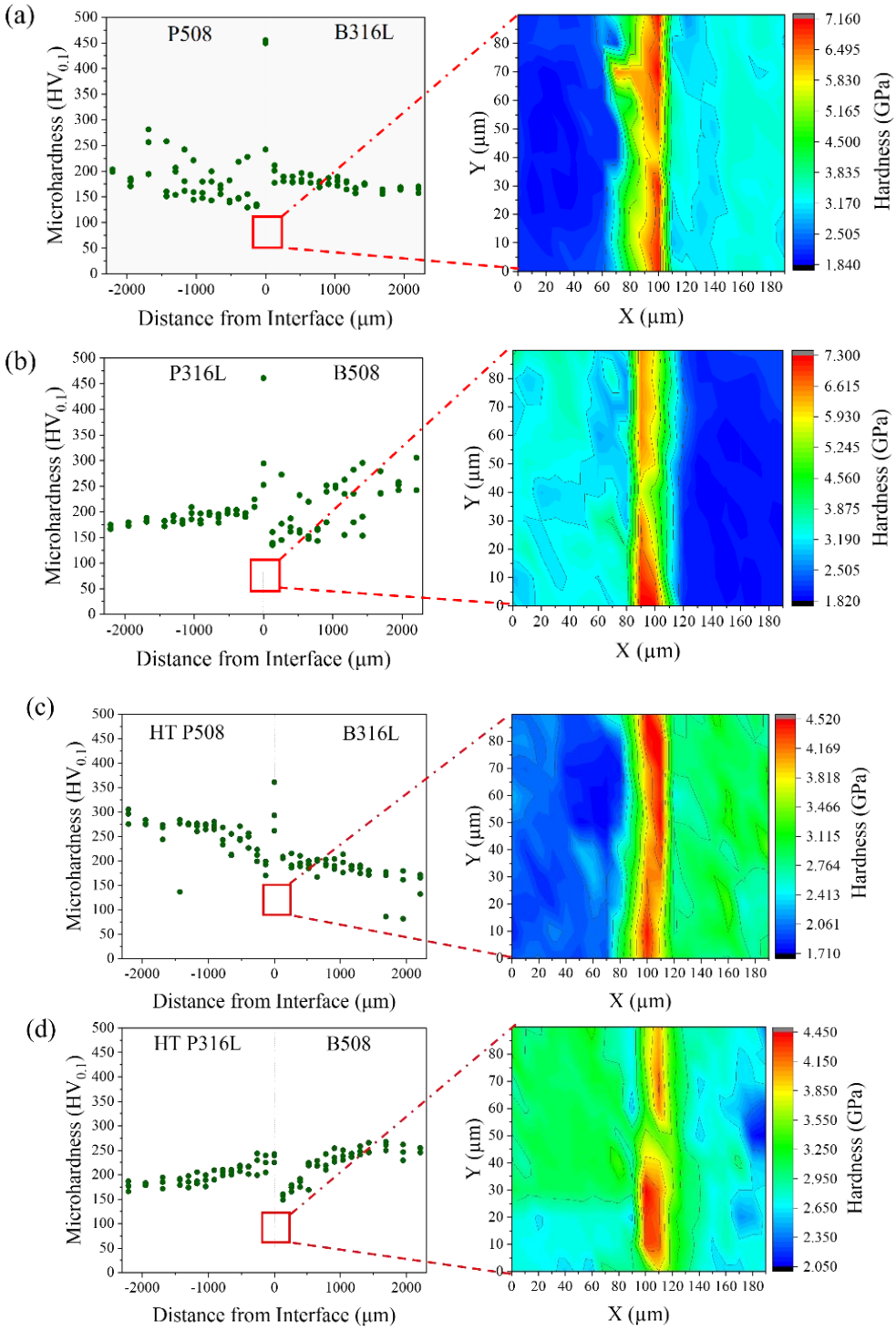

Figure 14. Microhardness and nano hardness results for as-received (a) P508-B316L (b) P316L-B508; SA+N+T (650ºC) (b) P508-B316L and (d) P316L-B508.

3.5.2. SA+N+T

From figure 14(c-d). the micro-hardness of P508-B316L and P316L-B508 in at solution anneal + normalization + tempering (650^{o}C) showed consistent microhardness distribution across the parent material. Due to the microstructural evolution of ferrite and bainite to a 100 percent bainitic microstructure, P508 and B508 exhibited uniformity. The average microhardness of P508 and B508 was 276 HV and 254 HV, respectively. In comparison, the average Vickers hardness of P316L and B316L was 190HV and 203HV, respectively. From figure 8. grain refinement occurred for both joint designs after heat treatment. After heat treatment, grain refinement occurred for both joint designs. Due to the Hall-Petch effect, the resulting data demonstrate an increase in the hardness of both parent materials.

4.5.3. Cause of Hard Interface

The interface was observed to have the highest microhardness among all samples. As stated previously, PM-HIP enhanced the interdiffusion as a result of the high processing temperature, resulting in the atomic migration of C and Fe from LAS to ASS. Ni and Cr, in contrast, diffuse from austenitic steel into low alloy steel. The formation of carbide precipitates was determined by the rate of cooling. Jang et al. investigated the effects of carbide formation for slow and fast cooling rates; he discovered that increased cooling rates produced fine carbide precipitates, while slow cooling coarsened the carbides [28]. Carbide formation occurred as a result of the migration of carbon and the influence of slow furnace cooling for the as-received condition. The diffusion of carbon on 316L and SA508 produced carbon-rich and carbon-poor zones, respectively. Nano-indentation mapping confirmed this in all cases. According to the data, the peak microhardness of as-received P508-B316L and P316L-B508 was 461 HV and 454.9 HV, respectively. The interface

microhardness of P508-B316L decreased from 461 HV to 363 HV and P316L-B508 reduced from 454.9 HV to 248 HV after heat treatment. In addition, fine carbides were observed across the interface of the as-received specimens, which became spheroidized cementite following heat treatment. Due to the change in carbide morphology and size, the microhardness at the interface decreased.

Chapter 5: Discussion

5.1. Microstructural origins of reduced toughness at the interface

Ferritic low alloy steel to austenitic SS joint's toughness is dependent on the size and volume fraction of oxide inclusions. By reducing the oxygen content by vacuum annealing at 600^{o}C and 900^{o}C, Gandy et al. found that the Charpy toughness value of A508 produced by PM-HIP increased from 99 J to 127, respectively [17]. As previously stated, the diameter of pure P508 oxide and P508-B316L oxide was 0.4 μm and 3 μm, respectively. The number density and growth of voids are dependent on the number of stress concentrators [29], which serve as crack propagation initiation sites. The joining of P508 and B316L decreased the toughness from 68J to 23J in comparison to pure P508. The presence of a greater number density and larger size of oxides at the P508-B316L interface led to a greater volume fraction of voids, thereby reducing the energy required for crack propagation. Likewise, pure P316L yielded an abundance of small oxides with an average size of 0.8 μm and exhibited a toughness of 169J. Cooper et al. performed a Charpy impact test and found that forged 304L had a toughness of 200 J higher than 304L manufactured by PM-HIP, whereas the oxygen content was 15 ppm and 110 ppm for forged and PM-HIP steel [19]. According to his findings, the low toughness was due to the presence of large oxides at the grain boundaries. From the results, it was concluded that the low toughness of P508-B316L was caused by the formation of coarse oxides located on the interface resulting in brittle fracture.

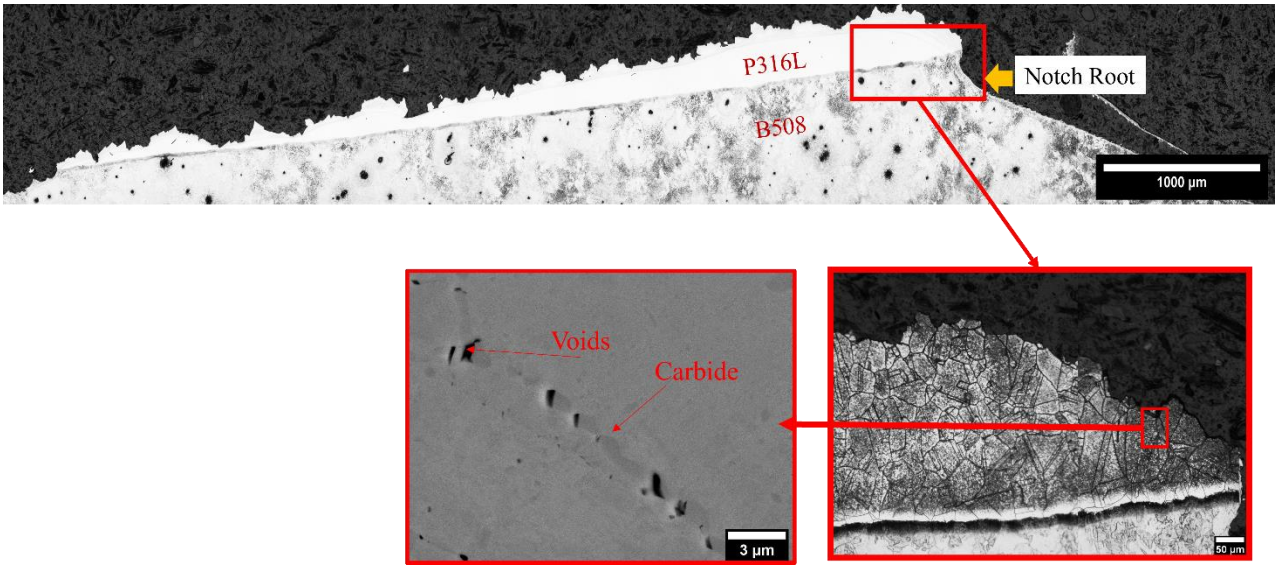

Figure 15. Cross-sectional optical and SEM images of fracture surface after the Charpy impact test for SA+N+T(650°C) condition for P316L-B508.

Figure 15 showed evidence that carbides precipitated along the grain boundary on the P316L side of B508. Similar to oxides, carbides reduce a material's toughness by acting as pinning sites that impede dislocation movement. S. Lee et al found that coarse M_3C carbides larger than the critical size were responsible for the reduction in fracture toughness for SA508 and fine M_2C carbides if homogenously distributed can improve fracture toughness [31]. The depicted carbides were adjacent to voids, which initiates microcracks that cleaved the carbides at the grain boundary.

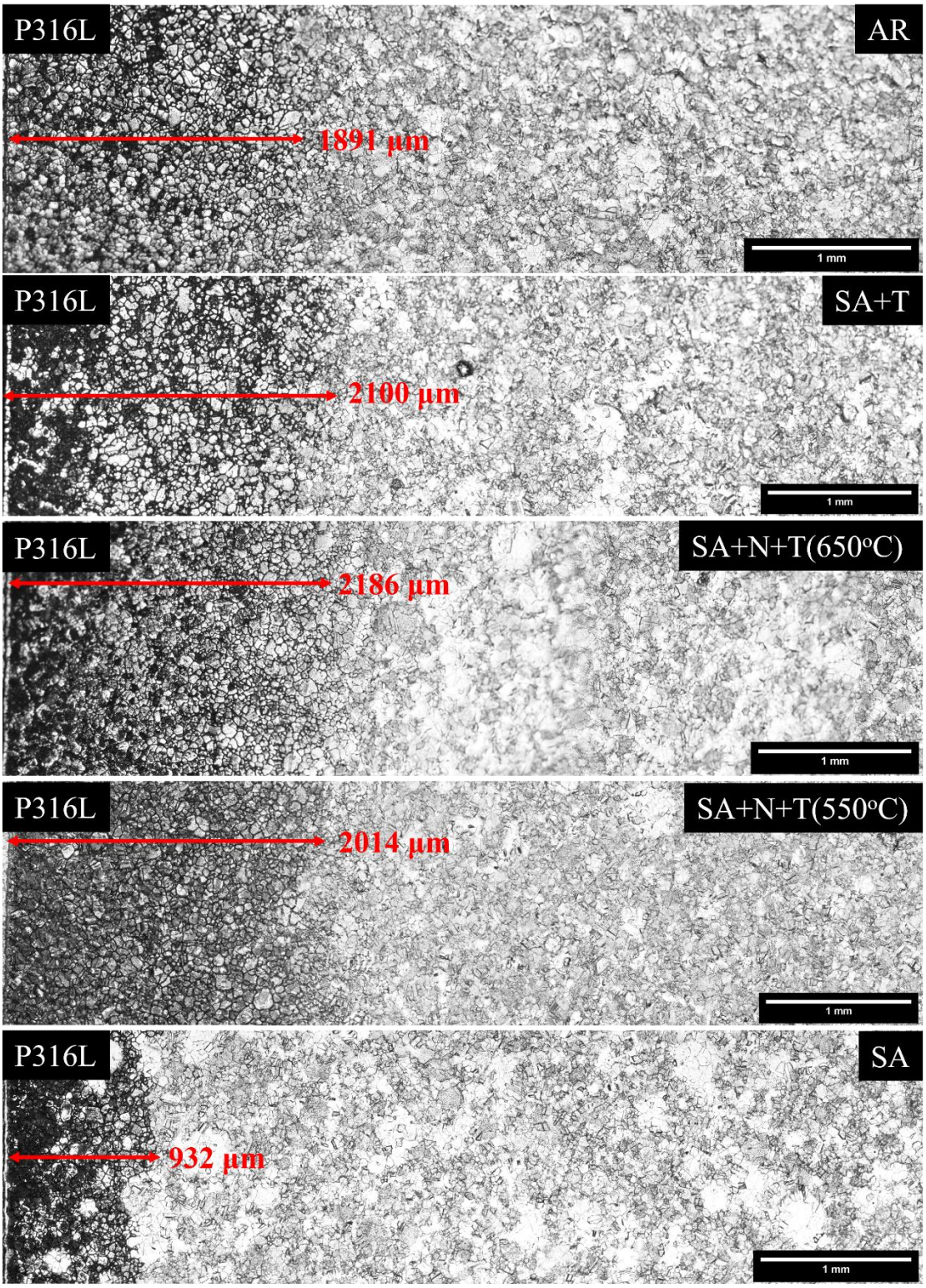

Figure 16. Optical images of sensitized samples of the dissimilar joint P316L at AR, SA, SA+T, SA+N+T(550ºC), and SA+N+T(650ºC) conditions.

5.2. Toughness vs Carbide Under Various Heat Treatments

The susceptibility to intergranular corrosion was studied by sensitization to find the extent of $M_{23}C_6$ carbide formation and the degree of sensitization. Figure 16 displays micrographs of the sensitization results at conditions: as-received, SA+T(650^{o}C), SA+N+T(650^{o}C), SA+N+T(550^{o}C), and SA at P316L side. The sensitization distances for the aforementioned conditions were 1891 μm, 2112.8 μm, 2185.8 μm, 2014.2 μm, and 931.8 μm, respectively. It was observed that the $M_{23}C_6$ carbides were present in the as-received conditions at a wide distance of 1891 μm. The precipitation of the carbides was due to the slow cooling rates during PM-HIP. The carbides were first dissolved at the HIP operational temperature of 1163^{o}C; however, due to the low cooling rates from furnace cooling, the carbides re-precipitated along the grain boundaries [33-34]. When the samples were subjected to solution annealing, the carbide extent was found to be highly sensitized and lowered by around 50 percent compared to the as-received state. This suggested that the solution annealing was not kept long enough to dissolve all of the carbides, as only half of the initial quantity was dissolved. Since carbide precipitation is time-dependent, it is possible that the holding time for the solution anneal was insufficient and that an additional 2h or more would have eliminated more carbides. In comparison, the SA+T, SA+N+T(650^{o}C), and SA+N+T(550^{o}C) resulted in a considerable extension of carbides when compared to the SA condition. This implied that the nucleation and proliferation of the carbides at the grain boundaries were due to the pre-existing carbides from the SA condition.

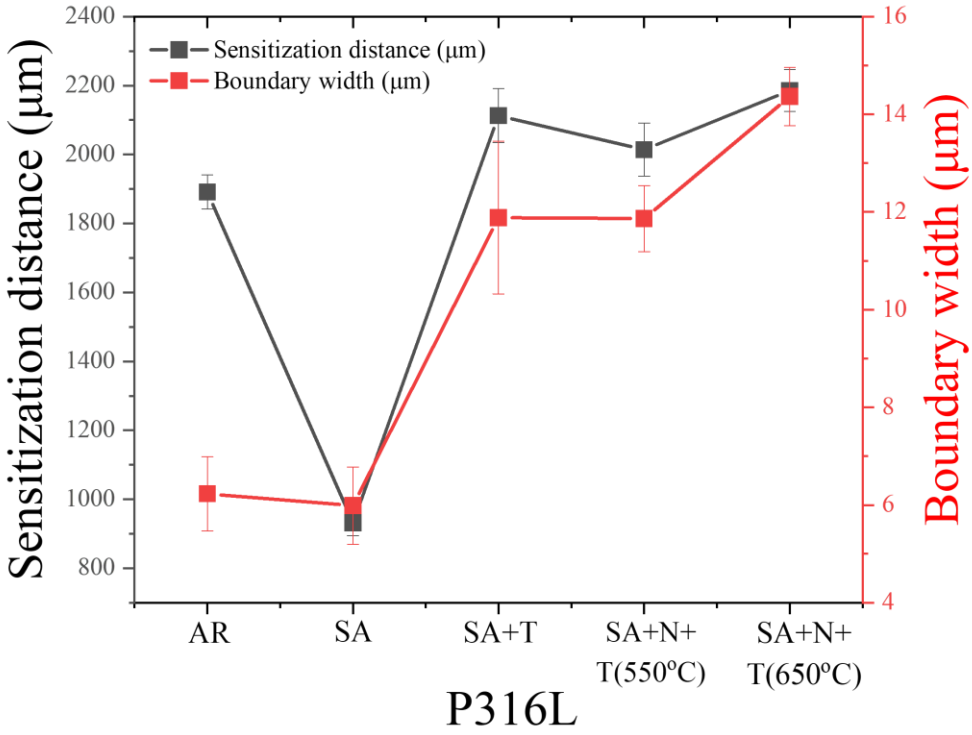

Figure 17. Sensitization results for dissimilar joint P316L at different heat treatment conditions for AR, SA, SA+T(650°C), SA+N+T(550°C), and SA+N+T(650°C).

Figure 17 illustrates the sensitization distance as a function of the boundary width for all the conditions and demonstrates how the sensitized grain boundary widths increased in size due to intergranular corrosion as heat treatment progressed. At 90 J, the SA condition exhibited the greatest toughness, which contributed to its short sensitization distance at 932 μm and low degree of sensitization at 6 μm. In comparison, sensitization distances were comparable at SA+N+T(650°C) and SA+N+T(550°C) conditions; however, toughness values were significantly different at 34.8 J and 57 J, respectively. At the SA+N+T(550°C) and SA+N+T(650°C), the boundary widths were 12 μm and 14 μm, respectively. The highest degree of sensitization was

found at SA+N+T(650°C) condition, which caused a higher volume fraction of $M_{23}C_6$ carbides to form located along the grain boundaries. This resulted in the low toughness of 34.8 J compared to 57 J compared to the SA+N+T(550°C) conditions, since the higher volume fraction of carbides depreciated the impact toughness which caused the cracks to propagate more easily.

5.3. Diffusion Simulation

5.3.1 316L to SA508

Figure 18. shows the simulated carbon content of 316L to SA508 by using PanDiffusion at the following conditions: as-received (1163°C-2h), SA (1065°C-2h), SA+N(900°C-2h)+T (650°C-4h), and SA+N+T (550°C-4h). Tables 3 and 4 list the alloy composition and thermal treatments, respectively. At all conditions, the carbon profile at 2000 μm away from the interface of 316L and 508 were constant. The carbon profile began to change rapidly when it was 1000 μm away from the interface and continued until it reached the interface. The inset shows the maximum carbon peaks for as-received, SA, SA+N+T(650°C), and SA+N+T(550°C) as 0.105 wt%, 0.107 wt%, 0.18 wt%, and 0.14 wt% C, respectively. Under all conditions, carbon was enriched on the P316L side and depleted on the SA508 side. Although, the carbon content peaks were the lowest at as-received and solution annealing conditions. The simulated results did not accurately represent the experimental sensitization data due to the pre-existing carbides. Comparatively, the tempering condition from 650°C to 550°C was observed to have reduced carbon peak from 0.18 wt% to 0.14 wt% C, respectively.

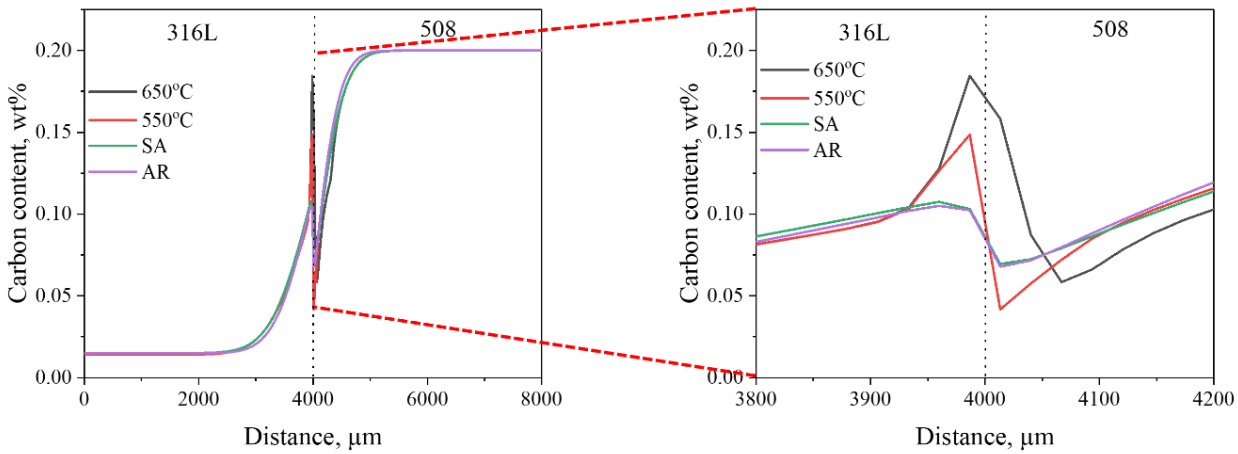

Figure 18. Simulated diffusion of the carbon content of 316L to SA508 at the following conditions: as-received, SA, SA+N+T(650°C), and SA+N+T(550°C).

Figure 19. illustrates the simulated extension and maximum $M_{23}C_6$ carbides across 316L to SA508. It is noted that $M_{23}C_6$ carbides were not present for as-received and solution-annealed conditions. At these conditions, only the Fcc phase existed. Since PanDiffusion calculates the phase from thermodynamic equilibrium it is not able to calculate the carbides formed from non-equilibrium conditions involved in slow cooling. From, the inset the $M_{23}C_6$ maximum carbides molar fractions were 3.7% and 2.3% for tempering at 650°C and 550°C. The change in carbides implied that tempering at 650°C displayed fast nucleation of carbides and tempering at 550°C showed sluggish nucleation. In comparison to the toughness data of tempering at 650°C and 550°C, there was an improvement when the tempering temperature was reduced. Hence, the reduction of carbides can lead to an improvement in toughness. Furthermore, the carbide extension was observed to exponentially increase until it was close to the interface. The simulation results showed a high formation of carbide precipitation at 500 μm away from the interface on the 316L side. By comparing the distance experimental sensitized sample of SA+N+T(650°C) at a sensitization

distance of close to 2200 µm. Although, the PanDiffusion does not take into account the carbides formed from non-equilibrium. The data from the simulation illustrates that the high carbide formation at the interface could not be fixed by heat-treatment optimization. Thus, it is not feasible to directly join P316L to B508 by PM-HIP even if the initial carbides are not present and will require a transitional joint between 316L and 508.

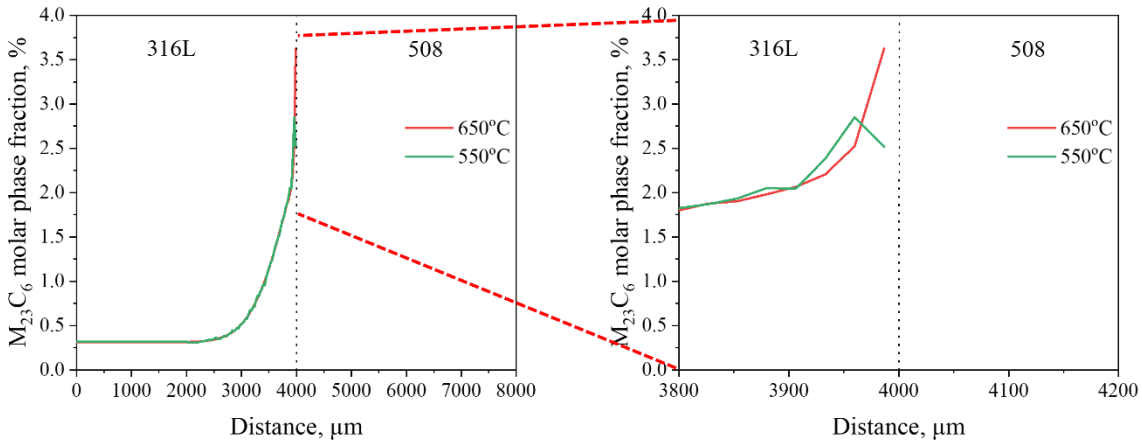

Figure 19. Simulated diffusion of $M_{23}C_6$ molar phase fraction of 316L to 508 at the following conditions: SA+N+T(650°C) and SA+N+T(550°C).

5.3.2 Ni-Based Alloy as a Transitional Material

Ni-based alloys are known to have a lower carbon diffusivity; by inserting Ni-alloy 600M or 82 between SA508 and 316L, the nucleation of carbides can be reduced. Figure 20 depicts the carbon profile and $M_{23}C_6$ carbide molar phase fraction of SA508-82-316L and SA508-600M-316L, which were simulated. As a transitional material, 600M and 82 carbon profiles exhibited comparable tendencies. In both instances, the carbon content of SA508 rapidly depreciates as it approaches the Ni-alloy, followed by a profile increase after passing the interface. The carbon then reaches a plateau and decreases further as it approaches the 316L interface. The $M_{23}C_6$ carbide

peaks for 600M and 82 were found to be 0.42 % and 0.37 %, respectively. Compared to simulation findings for 316L and SA508, these values were dramatically lowered. Utilizing 82 or 600M as a transitional material may be a viable option for reducing the concentration of $M_{23}C_6$ carbide at the interface of 316L. However, as this simulation only accounted for $M_{23}C_6$ carbide other detrimental carbides may form.

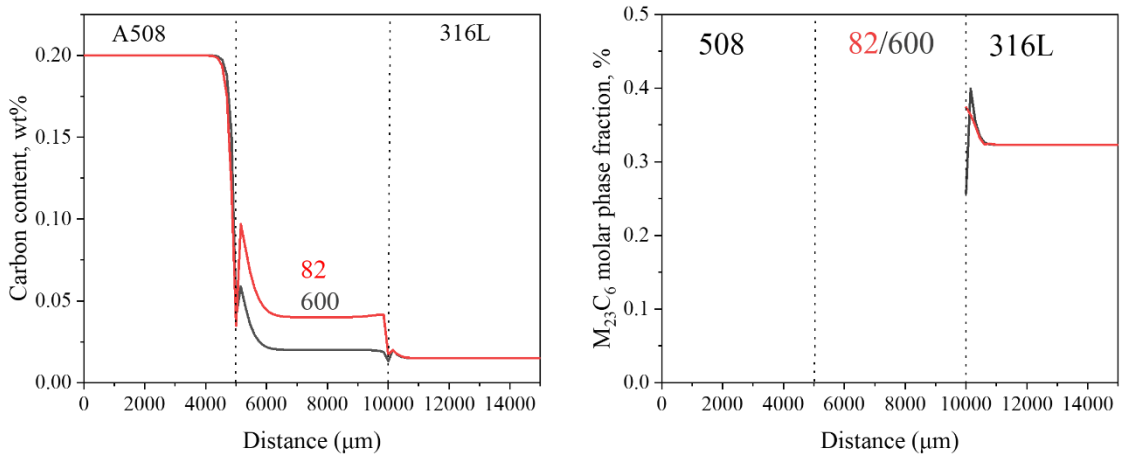

Figure 20. Simulated diffusion of 508 to 82/600M to 316L: a) carbon content, b) $M_{23}C_6$ molar phase fraction.

5.3.3 Functionally Graded Metal

By controlling the mixing ratios of powder 316L and powder SA508, a functionally graded composition can be employed as a transitional material to reduce the grain boundaries of $M_{23}C_6$ carbides. The maximal precipitation of mixed 316L+SA508 to SA508 and mixed 316L+SA508 to 316L is depicted in Figure 21. Using the mixing ratios of 316L and SA508 at 10% intervals and then balancing using SA508 created a compositional graded material. For 316L+508 to 508, the maximum $M_{23}C_6$ carbides were close to zero from 10% 316L to 50% 316L, with a slight rise at 60% 316L. A substantial increase occurred at 70% of 316L and decreased as the percentage of

316L reached 90%. In contrast, the carbide peaks for 316L to 316L+508 were initially high at 10% 316L and dropped linearly until 70% 316L. From 70% 316L to 90% 316L, the generation of carbides remained consistent at close to 0%. According to the data, the 50% to 60% 316L contained the lowest concentration of $M_{23}C_6$ carbides. Therefore, a ratio of 55% 316L to 45% SA508 was determined to be the optimal mixture to use. By reducing the carbide precipitation, it is possible to increase impact toughness by minimizing the degree of sensitization.

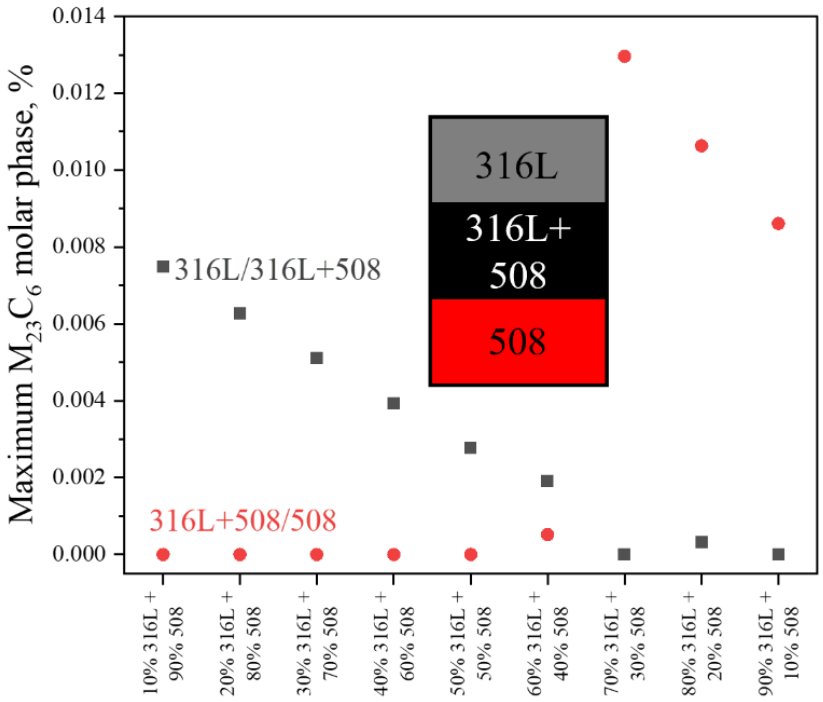

Figure 21. Simulated graded transition joint using 316L to graded 316L+508 and 508 to graded 316L+508.

Chapter 6: Conclusion

The joining of low alloy steel to austenitic SS in PM-HIP was found to be not feasible due to the low toughness at the interface. Although, the tensile properties were found to be satisfactory and the interfacial hardness was reduced. However, oxygen control was discovered to be crucial for P508 to prevent the precipitation of oxide inclusions at the interface of P508-B316L which contributed to its low toughness. Although P316L-B508 did not exhibit inclusions at the interface, the poor toughness was caused by the presence of $M_{23}C_6$ carbides located along the grain boundaries of P316L. Further heat treatment resulted in a higher sensitization distance due to the nucleation of pre-existing carbides and caused higher susceptibility to intragranular corrosion. To improve the impact toughness, PanDiffusion was used to optimize the heat treatment to find a heat treatment that contributed to the lowest precipitation of carbides. The reduction in tempering heat treatment led to slowed nucleation of carbides, but a high concentration of carbide persisted near the interface of 316L regardless of the heat treatment. It was determined that the carbide problem cannot be resolved by joining 316L directly to SA508, thus a transitional material is required. PanDiffusion was utilized to simulate the transitional material of SA508-600M-316L and SA508-82-316L as an alternative method to reduce carbon diffusivity. The two designs were found to significantly reduce the formation of the carbides; therefore, it could potentially improve the impact toughness and reduce the extent of sensitization. In addition, a functionally graded material design of 316L and SA508 at a ratio of 55% 316L to 45% SA508 was discovered to be another viable option for enhancing toughness.

References

[1] Nuclear Power in the USA - World Nuclear Association. Nuclear Power in the USA - World Nuclear Association. November 7, 2022. https://world-nuclear.org/information-library/country-profiles/countries-t-z/usa-nuclear-power.aspx#:~:text=The%20USA%20is%20the%20world's,worldwide%20nuclear%20generation%20of%20electricity.

[2] Frequently Asked Questions (FAQs) - U.S. Energy Information Administration. November 10, 2022. https://www.eia.gov/tools/faqs/faq.php.

[3] P.G. Tipping, Understanding and Mitigating Ageing in Nuclear Power Plants. Materials and Operational Aspects of Plant Life Management (PLIM). Woodhead Publishing Limited, 2010, ISBN: 978-1-84569-511-8

[4] Nuclear Essentials - World Nuclear Association, Nuclear Essentials - World Nuclear Association, Accessed November 10, 2022, https://www.world-nuclear.org/nuclear-essentials/are-there-different-types-of-reactor.aspx.

[5] G Yan, L. Han, C. Li, X. Luo, J. Gu, Characteristic of retained austenite decomposition during tempering and its effect on impact toughness in SA508 Gr.3 steel, Journal of Nuclear Materials, Volume 483, 2017, (2017) 167-175, https://doi.org/10.1016/j.jnucmat.2016.11.011.

[6] Pressurized Water Reactors, United States Nuclear Regulatory Commission, Accessed November 4, 2022, https://www.nrc.gov/reactors/pwrs.html

[7] A. Jenssen, K. Norrgaard, J. Lagerstroem, G. Embring, D. Tice, Assessment of cracking in dissimilar metal welds, Studsvik Report, (2001)

[8] A. Reichardt, A. A. Shapiro, R. Otis, R. P. Dillon, J. P. Borgonia, B. W. McEnerney, P. Hosemann, A. M. Beese, Advances in additive manufacturing of metal-based functionally graded materials, International Materials Reviews, (2021)1-29, https://doi.org/10.1080/09506608.2019.1709354

[9] Z. Sun, R. Karppi, The application of electron beam welding for the joining of dissimilar metals: an overview, Journal of Materials Processing Technology, Volume 59, Issue 3, 1996) 257-267, https://doi.org/10.1016/0924-0136(95)02150-7

[10] E. Stavroulakis, S. Irukuvarghula, E. Pickering, D. Stewart, M. Preuss, Fundamental aspects of functional grading via powder hot isostatic pressing – Development of microstructure and diffusional processes, Materials & Design, Volume 215, (2022), https://doi.org/10.1016/j.matdes.2022.110437

[11] J.R. Weeks, B. Vyas, H.S. Isaacs, Intergranular stress corrosion cracking of sensitized stainless steel, Brookhaven National Laboratory, (1975)

[12] J.C. Lippold, D.J. Kotecki, Welding Metallurgy and Weldability of Stainless Steel, 5th ed. John Willey & Sons, USA (2005), https://doi.org/10.1002/9781118960332

[13] Y. Yang, L. Li, Microstructure Evolution of Fine-Grained Heat-Affected Zone in Type IV Failure of P91 Welds, Welding journal (2016) 27-36, Welding Journal 95(1):27-36

[14] R. L. Reid, D. A. Copinger, V. S. White, U.S. Nuclear Power Plant Operating Cost and Experience Summaries, Oak Ridge National Laboratory, (2003)

[15] D. Herzog, K. Bartsch, B. Bossen, Productivity optimization of laser powder bed fusion by hot isostatic pressing, Additive Manufacturing, Volume 36, (2020) 2214-8604, https://doi.org/10.1016/j.addma.2020.101494.

[16] H.V. Atkinson, S. Davies, Fundamental aspects of hot isostatic pressing: An overview. Metallurgical and Materials Transaction A, (2000) 2981–3000, https://doi.org/10.1007/s11661-000-0078-2

[17] D. Gandy, K. William, B. William, V. Samarov, T. Miles, H. Steven,Assessment Of Powder Processing Methods For Production Of A Small Modular Reactor Vessel Component Assemblies Via Powder Metallurgy-HIP, IASMiRT, (2019) https://www.lib.ncsu.edu/resolver/1840.20/37956

[18] T. Shiokawa, M. Okuwaki, H. Urakawa, Y. Nagamachi, G. Triani, HIP process of a valve body to near-net-shape using grade 91 powder, Materials Research Forum LLC, (2019) 58-64, http://dx.doi.org/10.21741/9781644900031-8

[19] A. J. Copper, N.I. Copper, A. Bell, J. Dhers, A.H. Sherry, A Microstructural Study on the Observed Differences in Charpy Impact Behavior Between Hot Isostatically Pressed and Forged 304L and 316L Austenitic Stainless Steel, Metall Mater Trans A 46, (2015) 5126–5138, https://doi.org/10.1007/s11661-015-3140-9

[20] Y. Duan, W. Liu, Y. Ma, Q. Cai, W. Zhu, J. Li, Microstructure characterization and tensile properties of hot isostatic pressed China ultrahigh strength steel, Journal of Materials Research and Technology, (2020) 15192-15201, https://doi.org/10.1016/j.jmrt.2020.10.013.N/a

[21] B. Sutton, D. Gandy, Assessment of Powder Metallurgy-Hot Isostatic Pressed Nozzle-to-Safe End Transition Joints, Proceedings of the ASME 2017 Pressure Vessels and Piping Conference. Volume 6A: Materials and Fabrication, (2017), https://doi.org/10.1115/PVP2017-65776

[22] D. T. Hoelzer, The Use of Powder Metallurgy and Hot Isostatic Pressing for Fabricating Components of Nuclear Power Plants, (2022), ORNL/SPR-2022/2421

[23] X. Zhou, J. Dong, Y. Liu, C. Liu, L.Yu, Y. Huang, H. Li, Austenite to polygonal-ferrite transformation and carbide precipitation in high strength low alloy steel. International Journal of Materials Research, (2017) 12-19, https://doi.org/10.3139/146.111454

[24] G.E. Totten, Steel Heat Treatment: Metallurgy and Technologies (1st ed.), CRC Press, (2006), https://doi.org/10.1201/NOF0849384523

[25] F.G. Caballer, H. Roelofs, S. Hasler, C. Capdevila, J. Chao, J. Cornide, C.G. Mate, Influence of bainite morphology on impact toughness of continuously cooled cementite free bainitic steels, Materials Science and Technology, (2012) 95-102, https://doi.org/10.1179/1743284710Y.0000000047

[26] N. Jia, Y. Shen, Y.F. Liang, X.W. Feng, Nanoscale spheroidized cementite induced ultrahigh strength-ductility combination in innovatively processed ultrafine-grained low alloy medium-carbon steel, Sci Rep **7**, (2017), https://doi.org/10.1038/s41598-017-02920-9

[27] A.J. Copper, N.I. Copper, J. Dhers, A.H. Sherry, Effect of Oxygen Content Upon the Microstructural and Mechanical Properties of Type 316L Austenitic Stainless Steel Manufactured by Hot Isostatic Pressing. Metall Mater Trans A 47, (2016) 4467–4475 (2016). https://doi.org/10.1007/s11661-016-3612-6

[28] K.N. Jang, T.K. Kim, K.T. Kim, The effect of cooling rates on carbide precipitate and microstructure of 9CR-1MO oxide dispersion strengthened(ODS) steel, Nuclear Engineering and Technology, (2019) 249-256, https://doi.org/10.1016/j.net.2018.09.021.

[29] M. F. Horstemeyer, A. M. Gokhale, A void–crack nucleation model for ductile metals, International Journal of Solids and Structures, (1999) 5029-5055, https://doi.org/10.1016/S0020-7683(98)00239-X.

[30] S. Lee, S. Kim, B Hwang, B.S. Lee, C.G. Lee, Effect of carbide distribution on the fracture toughness in the transition temperature region of an SA 508 steel, Acta Materialia, (2002) 4755-4762, https://doi.org/10.1016/S1359-6454(02)00313-0.